Quantifying differences between passive and task-evoked intrinsic functional connectivity in a large-scale brain simulation

Antonio Ulloa[1,2]* and Barry Horwitz[1]

[1]Brain Imaging and Modeling Section, National Institute on Deafness and Other Communication Disorders, National Institutes of Health, Bethesda, MD, USA

[2]Neural Bytes, Washington, DC, USA

*Corresponding author

Email: antonio.ulloa@alum.bu.edu

Abstract

Establishing a connection between intrinsic and task-evoked brain activity is critical because it would provide a way to map task-related brain regions in patients unable to comply with such tasks. A crucial question within this realm is to what extent the execution of a cognitive task affects the intrinsic activity of brain regions not involved in the task. Computational models can be useful to answer this question because they allow us to distinguish task from non-task neural elements while giving us the effects of task execution on non-task regions of interest at the neuroimaging level. The quantification of those effects in a computational model would represent a step towards elucidating the intrinsic versus task-evoked connection. Here we used computational modeling and graph theoretical metrics to quantify changes in intrinsic functional brain connectivity due to task execution. We used our Large-Scale Neural Modeling framework to embed a computational model of visual short-term memory into an empirically derived connectome. We simulated a neuroimaging study consisting of ten subjects performing passive fixation (PF), passive viewing (PV) and delay match-to-sample (DMS) tasks. We used the simulated BOLD fMRI time-series to calculate functional connectivity (FC) matrices and used those matrices to compute several graph theoretical measures. After determining that the simulated graph theoretical measures were largely consistent with experiments, we were able to quantify the differences between the graph metrics of the PF condition and those of the PV and DMS conditions. Thus, we show that we can use graph theoretical methods applied to simulated brain networks to aid in the quantification of changes in intrinsic brain functional connectivity during task execution. Our results represent a step towards establishing a connection between intrinsic and task-related brain activity.

INTRODUCTION

Recently, there has been significant interest in investigating the relationship between intrinsic and task-evoked brain activity. This interest is driven by the potential to discover information contained in intrinsic brain activity that would reveal the repertoire of functional brain networks used to execute goal-directed tasks (Cole, Bassett, Power, Braver, & Petersen, 2014). Intrinsic and task-evoked activity are strongly interdependent (Bolt, Anderson, & Uddin, 2017) and understanding this interdependence holds the promise of providing a link between resting state and task-based empirical findings (Cole et al., 2014). Furthermore, the establishment of a clear relationship between intrinsic and task brain activity would allow the mapping of task-related brain areas in patients unable to comply with such tasks (Branco et al., 2016; Liu et al., 2009)

Neuroimaging studies have shown that performance of a cognitive task alters the intrinsic functional connectivity in non-task related brain regions (Bluhm et al., 2011; Tommasin et al., 2017; Vatansever, Menon, Manktelow, Sahakian, & Stamatakis, 2015). Bluhm and colleagues, for example, found increases in functional connectivity between two “default network” brain regions (posterior cingulate / precuneus and medial prefrontal cortex) and the rest of the brain during a visual working memory task as compared to a passive fixation task. In another study, Tommasin and colleagues found reductions in functional connectivity between brain regions within the “default mode network” (DMN) during an auditory working memory task as compared to an eyes-open resting state (RS) task. Similarly, Vatansever and colleagues found

reductions in functional connectivity within DMN brain regions during a motor task as compared to a RS task.

A very powerful tool that has been used to quantify changes in intrinsic functional connectivity due to task execution employs graph theoretical methods (Adams, Shipp, & Friston, 2013; Bolt, Nomi, Rubinov, & Uddin, 2017; Cohen & D'Esposito, 2016; Fuertinger, Horwitz, & Simonyan, 2015; Krienen, Yeo, & Buckner, 2014; Moussa et al., 2011). Graph theoretical metrics have been used in the last decade to study functional and structural brain networks as they provide ways to quantify both global network organization and local network properties (Bolt, Nomi, et al., 2017; Rubinov & Sporns, 2010).

A recent computational study (Lee, Bullmore, & Frangou, 2017) demonstrated the reliability of graph theoretical metrics obtained from simulated intrinsic brain activity. Lee and colleagues modeled brain regions as Kuramoto oscillators coupled by weights extracted from a structural connectome (Hagmann et al., 2008). After finding an optimal functional connectivity matrix (one that resembled the RS empirical connectivity matrix), they set out to compute global and local network metrics and compared them to empirically-obtained graph metrics during the resting state. They found that simulated brain activity can be reasonably used to model graph theoretical metrics of brain organization.

However, there is a need to test the use of graph theoretical metrics on simulated intrinsic activity during task execution. We aimed to use computational modeling and graph theoretical metrics to quantify differences in intrinsic functional brain connectivity of non-task-related

brain regions due to increasing task demands. We used a large-scale computational model of visual processing (Horwitz et al., 2005; Tagamets & Horwitz, 1998; Ulloa & Horwitz, 2016) embedded in a structural connectome (Hagmann et al., 2008) to examine differences in intrinsic neural activity between three conditions: passive fixation (PF), passive viewing (PV), and a visual delayed match-to-sample (DMS) task. Specifically, we set out to investigate whether computational modeling and graph theoretical metrics could be used to quantify and understand intrinsic neural activity changes in non-task brain regions due to increasing task demands.

RESULTS

To perform the current study, we embedded a biologically realistic model of visual short-term memory (Tagamets & Horwitz, 1998), shown in Figure 1, into an anatomical skeleton defined by a 998-node structural connectome (Hagmann et al., 2008), shown in Figure 2, using a blend of our large-scale neural model (LSNM) simulator (Ulloa & Horwitz, 2016) and the Virtual Brain (TVB) simulator (Sanz Leon et al., 2013). The visual short-term memory model comprises brain regions that are directly involved in performing a delayed match-to-sample (DMS) task for visual objects. The structural connectome was added to provide neural noise to the simulated neural activity during the DMS task, and in return, to receive inputs back from the DMS task nodes. We have described our framework in a previous paper (Ulloa & Horwitz, 2016) where we focused on the fMRI BOLD signal generation during the DMS task. In the current work, we sought to analyze the FC configurations in brain regions not driving task execution. These 'non-task' brain regions exhibit intrinsic activity and because of their reciprocal connections with

task-specific brain regions, their neural activity can potentially be modulated during task execution.

We generated ten virtual subjects by randomly varying the connection weights among brain regions in the structural visual model (see Methods section for details). We created three experimental conditions: passive fixation (PF), during which simulated subjects with a low "task signal" (roughly equivalent to subjects' attention level during task execution, but see Methods for definition of this parameter) are fixating on a small dot; passive viewing (PV), during which subjects passively look at visual shapes; and a DMS task, during which subjects compared two shapes presented within 1.5 seconds of each other and responded whether the second shape matched the memory of the first. Each simulated subject performed one 198-second experiment that consisted of 3-trial blocks interspersed with rest blocks (see Methods section for details).

Changes in BOLD activity of non-task brain regions due to different task conditions.

Figure 3 shows typical (averaged across neuronal populations within each brain region) neuronal activity for each condition for task-related brain regions during one trial. Figure 3 shows the task regions increasing activity due to both stimuli presentation (V1, V4, IT, PF), short-term memory maintenance (D1, D2), and response (FR). This increase occurs in the PV and DMS conditions (green and red lines) but not in the PF condition (blue line). Thus, the stimulus used in the PF condition (a small dot) does not generate visible changes in the neuronal activity of task regions. The details of the task-related responses shown in Figure 3

have been discussed in detail in previous papers (Horwitz et al., 2005; Ulloa & Horwitz, 2016). Figure 4 shows the BOLD signal averaged across those brain regions with direct anatomical connections to task regions. Figure 2 shows a graphical depiction of the non-task nodes that are directly connected to task nodes. Notice how BOLD activity increases during the task blocks (shaded areas) and how they do so more prominently during DMS than during PV and during PV than during PF. Also notice how that BOLD activity change is larger for some of the brain regions with direct connections to IT, FS, D1, D2, FR than those regions with direct connections to V1 and V4. This is due to variations in the strength of the connecting weights from task-related nodes to non-task nodes. As we can see in Figure 4, changes in all task-related brain regions correlate with BOLD signal changes in non-task brain regions directly connected to them.

Intrinsic FC differences between PF, PV and DMS conditions.

We computed FC matrices for the three simulated conditions and for all subjects. Figure 5 shows across-subject averages of FC matrices for the three conditions. Figure 6 shows scatter plots between PF and PV and between PF and DMS conditions. As shown in Figure 6, the correlation coefficients between PF and both PV and DMS were high (0.90 and 0.83, respectively), demonstrating only small differences in the pair-wise consistency of functional connections across conditions. As noted above, these correlation matrices consist only of connectome nodes (e.g., no LSNM task-based nodes were used to construct these matrices). In summary, there were small changes in the pair-wise functional connectivity between PF and PV and between PF and DMS conditions.

143

144 **Graph theoretical metrics of PF, PV, and DMS conditions.**

145 Using graph theoretical methods (Rubinov & Sporns, 2010), we computed eight network
146 metrics (see Methods section for definition of each metric): global and local efficiencies,
147 average clustering coefficient, characteristic path length, eigenvector centrality, betweenness
148 centrality, participation coefficient, and modularity. We calculated these metrics using
149 weighted FC matrices for a range of plausible threshold densities (Di, Gohel, Kim, & Biswal,
150 2013). Figure 7 shows across-subject averages of those metrics for a range of network densities
151 (Di et al., 2013). Figure 7 shows that as the task changed from PF to PV to DMS, there was an
152 increase in global efficiency, local efficiency, average clustering coefficient and average
153 betweenness centrality (mostly at the lowest threshold studied, 5%), and modularity.
154 Conversely, as the task changed from PF to PV to DMS, there was a decrease in average
155 characteristic path length, average eigenvector centrality, and average participation coefficient.

156

157 **Differences in graph metrics between PF and PV and between PF and DMS.**

158 For each graph metric obtained, we computed the relative difference (see Methods section for
159 details) between PF and PV and between PF and DMS (see Figure 8). We observed significant
160 differences between PF and PV and between PF and DMS in modularity (54.2 $\pm$ 8% and 81.3 $\pm$
161 11.6%, respectively), eigenvector centrality (16.3 $\pm$ 1.7% and 22.1 $\pm$ 1.8%, respectively) and
162 clustering coefficient (7.9 $\pm$ 1.3% and 12.7 $\pm$ 2%); smaller changes in global efficiency (1.7 $\pm$
163 0.2% and 2.4 $\pm$ 0.3), local efficiency (2.2 $\pm$ 0.3% and 3.2 $\pm$ 0.4%), characteristic path length (1.7

164 $\pm$ 0.1% and 2.3 $\pm$ 0.3%), betweenness centrality (1.6 $\pm$ 0.3% and 2.6 $\pm$ 0.4%), and participation

165 coefficient (0.2 $\pm$ 0.1% and 0.4 $\pm$ 0.1%).

166

167 **Differences in modularity between conditions.**

168 To further visualize the large differences in modularity configurations during the three

169 simulated conditions, we rendered the binary FC network in each condition as connection space

170 graphs using Gephi (Bastian, Heymann, & Jacomy, 2009); www.gephi.org). We used the

171 algorithm of Blondel et al (Blondel, Guillaume, Lambiotte, & Lefebvre, 2008) to find the

172 modularity at a density threshold of 10%. Figure 10 shows connection space graphs displayed

173 on a radial axis layout (axis have a slight spiral to improve visualization of inter-module

174 connectivity). Nodes that belong to the same module are represented by the same color and

175 group together on the same radial axis. The connections between nodes have the color of the

176 node where those connections originate. We can see a decrease in the number of modules,

177 from 8 in PF to 6 in PV to 3 in DMS and an increase in modularity (see increase in modularity

178 graph in Figure 7). The increase in modularity from PF to PV to DMS means that the functional

179 network rearranges itself into fewer modules with more functional connections between nodes

180 within the same module (compare the very clearly defined modules in DMS versus PF and DMS

181 versus PV in Figure 10). We emphasize again that these results refer to non-task related nodes.

182

183 **DISCUSSION**

184 Using a large-scale computational model of visual short-term memory embedded into an

185 anatomical connectome, we compared simulated intrinsic brain activity of non-task related

186 brain regions during three tasks: passive fixation (PF), during which simulated subjects with a
187 low "task signal" or "attention" level are fixating on visual stimuli (a small dot); passive viewing
188 (PV), during which subjects passively watch changing visual shapes but take no action; and a
189 DMS task, during which subjects compared two shapes presented within 1.5 seconds of each
190 other and responded whether the second shape matched the memory of the first. The PF
191 condition may be considered equivalent to a resting state condition as a passive fixation task
192 has been often used in RS fMRI studies. The key difference between the PF and the PV
193 conditions was that the stimulus during the PF condition was an unchanging small dot whereas
194 in the PV condition several different and larger stimuli were presented. The key difference
195 between the PV and the DMS conditions was the level of the "task" or attention signal, which
196 was set to a low level in the PV condition and to a high level during the DMS condition. As
197 discussed in the Methods section, the task signal level determines whether an input stimulus is
198 going to be retained in short-term memory (Horwitz et al., 2005). Additionally, because of
199 feedback connections from D1 in prefrontal cortex to IT and V4 (see model diagram in Figure 1),
200 the task signal level indirectly influences neuronal activity in V1, V4, and IT (compare neuronal
201 activity in V1, V4, and IT during different conditions in Figure 3).
202
203 To quantify differences between PF, PV and DMS conditions, we used pair-wise temporal
204 Pearson correlations (FC matrices) and graph theory metrics of fMRI FC matrices. Whereas we
205 found small differences between the FC matrices of the simulated conditions, these differences
206 we not particularly impressive. However, we found clear-cut differences in each of the graph
207 theory metrics: Graded increases from PF to PV to DMS in global efficiency, local efficiency,

clustering coefficient, betweenness centrality and modularity; and graded decreases in the from PF to PV to DMS in characteristic path length, eigenvector centrality, and average participation coefficient. Our simulated graph theory results largely agreed with empirical studies.

In our computer simulations, the intrinsic brain activity across different conditions is modulated by ongoing neural activity in brain regions engaged in each task (task brain regions). This modulation happens through the strength of the anatomical connections of those brain regions to the rest of the brain (non-task brain regions, see Figure 2).

When the brain engages in a behavioral task, the activity in neuronal populations driving the task has the potential of reverberating throughout the brain, thereby altering the intrinsic neural activity of neuronal populations not involved in the task. A crucial question is whether one can quantify those changes in intrinsic functional connectivity. Computational modeling can be useful in this regard, as it allows us to isolate non-task from task neuronal populations and to convert simulated synaptic activity into neuroimaging time-series which in turn can be converted to FC matrices.

A commonly used method to simulate the resting state is by modeling local neuronal populations with oscillators and using the structural connections obtained from diffusion tractography as connection weights between the model neuronal populations. A parameter search is then conducted to find a global coupling parameter and a white matter conduction

speed producing a simulated FC matrix that best matches an empirical FC matrix (Cabral, Hugues, Sporns, & Deco, 2011; Ghosh, Rho, McIntosh, Kotter, & Jirsa, 2008; Gilson, Moreno-Bote, Ponce-Alvarez, Ritter, & Deco, 2016; Hansen, Battaglia, Spiegler, Deco, & Jirsa, 2015; Honey et al., 2009; Lee et al., 2017; Roy et al., 2014; Sanz-Leon, Knock, Spiegler, & Jirsa, 2015). This is the method we used to generate intrinsic activity in the "rest of the brain" of our simulations.

Consistency of pair-wise functional connectivity across task conditions

There was a high correlation between the pairs in the FC connectivity matrices between PF and PV and between PF and DMS (Figure 6). Several researchers have used pair-wise spatial correlations between functional connectivity (FC) matrices to compare intrinsic to task-evoked conditions (Bolt, Nomi, et al., 2017; Buckner et al., 2009; Cohen & D'Esposito, 2016; Cole et al., 2014; Di et al., 2013; Krienen et al., 2014; Smith et al., 2009). Generally, there is a relatively high spatial correlation (i.e., 0.64 – 0.9) between a passive condition (such as visual fixation or eyes closed, which are often used to study intrinsic brain activity) and a task condition. Despite such high correlations, differences do exist between passive and task FC, and those differences may be attributable to functional modifications that allow the brain to focus on performing a given task (DeSalvo, Douw, Takaya, Liu, & Stufflebeam, 2014; Di et al., 2013; Tomasi, Wang, Wang, & Volkow, 2014).

Bolt and colleagues (Bolt, Nomi, et al., 2017) recently showed that one can have largely consistent FC between passive and task conditions, and at the same time have largely different

whole-brain graph theoretical metrics between passive and task conditions. However, a description of the mechanisms behind those seemingly divergent results has not yet been provided.

Increases in Global Efficiency

Our study resulted in higher global efficiency for DMS than for PV and for PV than for PF. During the simulated PF condition, the stimuli used is small and mostly activates V1/V2 and V4 and IT areas to a small degree (blue lines in Figure 3), During the PV condition, the larger stimuli used causes an increase of neuronal activity in V1/V2, V4, IT, FS, D1, D2, FR (as shown in the trial time-series of Figure 3, green lines), thereby contributing to an increase in neuronal activity of non-task nodes directly connected to task nodes (see green lines in the shaded areas of the time-series in Figure 4). During the DMS condition, the neuronal activity across the task brain regions is higher than during the PV condition (red lines in Figure 3). This increase in neuronal activity of task brain regions contributes to an increase in neuronal activity of several of the non-task brain regions with direct connections to task regions during PV and DMS conditions as compared to PF condition (see Figure 4). As shown in the FC matrices of Figure 5, there is an increase in the correlation of several pair-wise connections from PF to PV to DMS. This increase in functional connectivity contributed to a consistent increase in global efficiency from PF to PV to DMS (Figure 7).

Graph theoretical measures in empirical studies have consistently shown higher global efficiency during task than during passive conditions (although this could depend on the

complexity of the task, but see (Cohen and D'Esposito 2016)). The global efficiency has been found to be higher during a task than during passive fixation (Bolt, Nomi, et al., 2017; Cohen & D'Esposito, 2016), higher during a task than during an eyes closed condition (Fuertinger et al., 2015), greater during a one-back visual memory task than during passive viewing and an eyes closed condition (Wen et al., 2015), and higher for coactivation studies than during RS (Di et al., 2013). In our simulations, the global efficiency is higher during DMS than during PV and PV. This is due to the short-memory task causing an increase of neural activity in brain regions that are in turn connected to a widely distributed network in the rest of the brain.

Increases in Local efficiency

Our simulations showed a greater local efficiency for DMS than for PV and for DMS than for PF. This is consistent with empirical studies showing an increase in local efficiency with increasing task demands (Wen et al., 2015).

Increases in Clustering Coefficient

Our simulations showed a greater clustering coefficient during DMS than during PV and during PV than during PF. Previous empirical studies have found a clustering coefficient that is greater for task than during passive fixation (Bolt, Nomi, et al., 2017), lower during a blend of activation studies than during resting state (Di et al., 2013), and greater during a language task than during eyes closed (Fuertinger et al., 2015).

Increases in characteristic path length

296 Our simulations showed smaller characteristic path length during DMS than during PV and
297 during PV than during PF. This is to be expected because as the global efficiency increases, the
298 characteristic path length decreases.
299
300 **Decreases in mean Eigenvector Centrality**
301 Our simulations showed smaller eigenvector centrality during DMS than during PV and during
302 PV than during PF. The eigenvector centrality metric provides a measure of how well connected
303 a given node is considering how well connected that node's neighbors are. Thus, eigenvector
304 centrality is recursive because a given node's eigenvector centrality depends on the node's
305 neighbors' eigenvector centrality. To get a more detailed view of the reason behind smaller
306 mean eigenvector centrality for more complex tasks (Figure 7), we rendered the eigenvector
307 centrality for each node on axial and sagittal views of the brain (Figure 9A). Figure 9A shows
308 that as the task complexity increases (from PF to PV to DMS) the eigenvector centrality
309 increases in a few nodes and decreases in most other nodes. Thus, on average the eigenvector
310 centrality decreases but the nodal eigenvector centrality in a few nodes increases as the task
311 complexity increases. Note that several of the nodes in which the eigenvector centrality
312 increases during PF and DMS are the nodes that are directly connected to task nodes (compare
313 to Figure 2). The reason the increases are concentrated on the right side of the brain is due to
314 the task nodes, which are embedded in the right side of the brain, having direct connections
315 mostly to the right side of the brain (see Figure 2). Compare the changes in eigenvector
316 centrality with the changes in betweenness centrality (Figure 7) which remain almost the same
317 during PF, PV and DMS (Figure 9B).

Increases in Betweenness Centrality

Our simulations show a higher betweenness centrality at the lower density threshold (5%) but the average betweenness centrality is very similar across all the other density thresholds (Figure 7). As mentioned above, the betweenness centrality at each individual node (Figure 9B) remains relatively constant across conditions. Previous empirical studies have shown a difference in nodal centrality when resting state and task are compared (Di et al., 2013).

Decreases in Participation Coefficient

Our simulations showed greater participation coefficient (in a predefined set of modules) for PF than for PV and for PV than for DMS (Figure 7). Participation coefficient measures each node participation in a set of predefined modules. We used the modules defined by Hagmann et al (Hagmann et al., 2008). Previous studies have shown a higher participation coefficient (between-module connectivity) during passive fixation than during a semantic task (DeSalvo et al., 2014).

Increases in Modularity

Our simulations showed a smaller modularity for PF than for PV and for PF than for DMS. Some empirical studies have found a greater modularity metric during RS than during a blend of activation studies (Di et al., 2013), and a greater modularity during passive fixation than during an n-back task using visually-presented phonemes (Cohen & D'Esposito, 2016). However, Cohen et al (Cohen & D'Esposito, 2016) found a similar modularity during passive fixation and a finger

tapping task. Other empirical studies have found that that the modularity varies as a function of performance, but here the evidence is also inconsistent. For example, Stevens et al (Stevens, Tappon, Garg, & Fair, 2012) found a positive correlation between RS modularity and visual working memory capacity and Meunier et al (Meunier et al., 2014) found a negative correlation between modularity and memory scores in an odor recognition task. Additionally, Yue et al (Yue et al., 2017) have found significant individual variability in modularity during resting state.

Related computational studies comparing resting state and task-based functional connectivity.

Two previous computational approaches have compared the intrinsic brain activity obtained during resting state versus the one obtained during task; however, none of those models was specifically concerned with quantifying intrinsic activity differences between different task conditions (which is the goal of our paper). The first one of those studies, by Ponce-Alvarez and colleagues (Ponce-Alvarez, He, Hagmann, & Deco, 2015) simulated RS using a set of mean field equations (excitatory-inhibitory pairs) interconnected by the anatomical connections of a 66-node connectome. A visual task was approximated by applying external stimulation (stationary inputs) to visual nodes during the RS simulation. Ponce-Alvarez's model revealed a decreased synaptic activity variability during the visual task as compared to the RS condition.

The second computational study comparing task versus rest (Cole, Ito, Bassett, & Schultz, 2016) similarly applied stationary inputs to a set of neighboring nodes in a simplified computational model to simulate six different tasks. Cole and colleagues used the FC strengths during a

362 passive task to predict the fMRI task activation of a held-out brain region. They did this for each
363 one of the brain areas simulated to produce a prediction of the fMRI activity in each one of the
364 brain areas simulated given a passive task FC matrix.
365
366 **Caveats and limitations of our study**
367 Different passive experimental conditions have been used in neuroimaging to study intrinsic
368 brain activity (also referred to as the "resting state (RS)") (Biswal, Yetkin, Haughton, & Hyde,
369 1995; Fox, Corbetta, Snyder, Vincent, & Raichle, 2006; Greicius, Krasnow, Reiss, & Menon,
370 2003). Three of the conditions most commonly used as a resting state condition are passive
371 fixation (PF), eyes open with no fixation, and eyes closed. Yan and colleagues (Yan et al., 2009)
372 found significantly higher FC in Default Mode Network (DMN) brain areas during eyes open
373 than during eyes closed condition. It is also important to emphasize that the functional
374 magnetic resonance (fMRI) results can vary depending on several other factors including: how a
375 RS task is defined (Van Dijk et al., 2010; Yan et al., 2009), which task instructions are given to
376 subjects (Benjamin et al., 2010), and whether subjects were engaged in a task prior to RS
377 (Waites, Stanislavsky, Abbott, & Jackson, 2005). Thus, whereas one can compare (within the
378 limitations outlined below) the results of our study with empirical studies using passive fixation,
379 our results cannot be directly extrapolated to all RS-fMRI studies.
380
381 One way in which the simulations presented here are different from our previous paper (Ulloa
382 & Horwitz, 2016) is that the model response units have been relocated from prefrontal cortex
383 to PreSMA. The relocation of the response units to PreSMA is based on an fMRI study by

384 (Pessoa, Gutierrez, Bandettini, & Ungerleider, 2002), who found an increase in BOLD fMRI in
385 the PreSMA area at the end of the delay period during a visual working memory task.
386 Additionally, a study by (Petit, Courtney, Ungerleider, & Haxby, 1998) has also demonstrated
387 BOLD fMRI activity in the PreSMA area during a working memory task. The relocation from
388 previous studies from our lab of the model response units to PreSMA makes biological sense as
389 it better reflects the complexity of the task we are trying to simulate. The identification of
390 realistic locations within the brain for each one of the model units is crucial as different
391 locations of task-related modules will modulate different non-task nodes in the connectome,
392 thereby producing different FC configurations.
393
394 One of the limitations of our study is that our model connectome does not have other sensory
395 systems apart from the visual system. Therefore, one should exercise caution when comparing
396 FC matrices of our simulation to empirical ones as the empirical ones would contain higher FC
397 that are the result of other sensory systems being activated by either intrinsic or extrinsic
398 processes. For example, in an fMRI scanner room, there is significant auditory stimulation
399 (scanner noise) as well as somatosensory input, which we have not simulated in the present
400 work.
401
402 In our simulations, we only embedded the visual model in the right hemisphere. As a result, the
403 intrinsic activity was mostly localized to the right hemisphere. Nonetheless, there were
404 significant intrinsic activity changes in the left hemisphere, and those were caused by structural
405 connectivity between both hemispheres.

406

407 Another limitation of our study is that the weights of the structural connectome used in this
408 paper are undirected and we assumed all connection weights to be excitatory. It is well known
409 that diffusion tractography has serious limitations as it produces a significant number of false
410 positives (Maier-Hein et al., 2017), has relatively low resolution and measures white tracts only
411 indirectly (Jbabdi, Sotiropoulos, Haber, Van Essen, & Behrens, 2015). Some researchers have
412 simulated whole brain activity using connectome datasets obtained from reconstructions of
413 retrograde tracer injections in macaques (Chaudhuri, Knoblauch, Gariel, Kennedy, & Wang,
414 2015) or a composite of diffusion spectrum imaging in humans and macaque tracer data (Sanz-
415 Leon et al., 2015). Despite the low resolution and lack of sign and direction of the human
416 tractography data, we decided to use it as it allowed the "brain regions" of our task based
417 simulator to be embedded into plausible locations within the structural connectome.

418

419 **CONCLUSIONS**

420 In conclusion, we used our large-scale neural modeling framework to quantitatively compare
421 neural dynamics of non-task brain regions during passive fixation, passive viewing, and a visual
422 short-term memory task. We were able to obtain quantitative measures of differences in
423 simulated functional connectivity by using graph theoretical methods. Our simulated graph
424 theory results largely agreed with experiments. We were also able to relate those network-level
425 changes to the underlying model mechanisms. We showed that we can use computational
426 modeling, functional connectivity and graph theoretical metrics to quantify changes in intrinsic
427 FC of non-task brain regions due to increasing task demands. Our work is relevant to the

characterization of intrinsic brain activity differences between passive and active task conditions and to the use of neural modeling in the design of empirical studies and the comparison of competing hypothesis of brain function.

METHODS

In the present work, we analyzed functional connectivity derived from BOLD fMRI time-series, calculated from simulated neural activity data using the framework presented in a previous paper (Ulloa & Horwitz, 2016). Whereas in our previous paper we evaluated the FC between brain regions directly involved in executing a task, in the present paper we examined the intrinsic FC in the rest of the brain (brain regions not involved in task execution). To better address that question, we performed a model parameter search to find a reasonable match between empirical and model FC. Below we briefly describe the components of the framework and how it was used to generate the simulated multi-subject experiment presented in this study. The source code of our modeling work, including simulation, analysis and visualization scripts, is freely available at https://nidcd.github.io/lsnm_in_python/.

Visual object processing model and The Virtual Brain

a. Visual object processing model

Our in-house visual (Tagamets & Horwitz, 1998) object processing model consists of interconnected neuronal populations representing the cortical ventral pathway that has been shown to process primarily the features of a visual object. This stream begins in striate visual cortex, extends into the inferior temporal lobe and projects into ventrolateral prefrontal cortex

(Haxby et al., 1991; McIntosh et al., 1994; Ungerleider & Mishkin, 1982). The regions that comprise the visual model include ones representing primary and secondary visual cortex (V1/V2), area V4, anterior inferotemporal cortex (IT), and prefrontal cortex (PFC) (see Fig. 1). Each of these regions contain one or more neural populations with different functional attributes (see caption to Fig. 1 for details). This model was designed to perform a short-term memory delayed match-to-sample (DMS) task during each trial of which a stimulus S1 is presented for a certain amount of time, followed by a delay period in which S1 must be kept in short-term memory. When a second stimulus (S2) is presented, the model must respond as to whether S2 matches S1. The model can also perform control tasks: passive fixation (PF) and passive perception of the stimuli (PV), in which no response is required. Multiple trials of the active and passive tasks constitute a simulated functional neuroimaging study.

The key feature used to define a visual object was shape. Model neurons in V1/V2 and V4 were assumed to be orientation selective (for simplicity, horizontal and vertical orientations were used). The structural submodels employed were based on known monkey neuroanatomical data. An important assumption for the visual model, inferred from such experimental data, was that the spatial receptive field on neurons increased along the ventral processing pathway (see (Tagamets & Horwitz, 1998) for details).

Each neuronal population consisted of 81 microcircuits, each representing a cortical column. The model employed modified Wilson-Cowan units (an interacting excitatory and inhibitory pair of elements for which spike rate was the measure of output neural activity) as the microcircuit (Wilson & Cowan, 1972). The input synaptic activity to each neuronal unit can

471 also be evaluated and combinations of this input activity were related to the fMRI BOLD signals
472 via a forward model.

473 In an earlier version of the model (Horwitz et al., 2005), half the neural populations
474 within the model were 'non task-specific' neurons that served as noise generators to 'task-
475 specific' neurons that processed shapes during the DMS task. The model generated time series
476 of simulated electrical neuronal and synaptic activity for each module that represents a brain
477 region. The time series of synaptic activity, convolved with a hemodynamic response function,
478 was then used to compute simulated fMRI BOLD signal for each module representing a brain
479 region, as well as functional connectivity among key brain regions (see (Horwitz et al., 2005) for
480 details on this method). This model was able to perform the DMS task, generate simulated
481 neural activities in the various brain regions that matches empirical data from non-human
482 preparations, and produces simulated functional neuroimaging data that generally agree with
483 human experimental findings (see (Tagamets & Horwitz, 1998) and (Horwitz et al., 2005) for
484 details). In the current paper, we employ the version of the model introduced by Ulloa and
485 Horwitz (Ulloa & Horwitz, 2016) in which non task-specific neurons are replaced by noise-
486 generated activity from neural elements in The Virtual Brain software simulator (Sanz Leon et
487 al., 2013).
488
489 *b. The Virtual Brain*
490 The Virtual Brain (TVB) software (Sanz Leon et al., 2013; Sanz-Leon et al., 2015) is a simulator of
491 primarily resting state brain activity that combines: (i) white matter structural connections
492 among brain regions to simulate long-range connections, and (ii) a given neuronal population

model to simulate local brain activity. It also employs forward models that convert simulated neural activity into simulated functional neuroimaging data. TVB source code and documentation are freely available from https://github.com/the-virtual-brain.

In the current paper, for the structural model, we chose the DSI-based connectome described by (Hagmann et al., 2008), which contains 998 nodes. For the neural model for each node, we employed Wilson-Cowan population neuronal units (Wilson & Cowan, 1972) to model the local brain activity because our in-house LSNM simulators use modified Wilson-Cowan equations as their basic neuronal unit. Our forward model that converts simulated neural activity into simulated fMRI is a modification of the Balloon-Windkessel model of Friston et al. (Friston, Mechelli, Turner, & Price, 2000; Stephan, Marshall, Penny, Friston, & Fink, 2007) that is included in the TVB.

Integrating TVB and LSNM

To perform our computational study, we concurrently ran two neural simulators: Our Large-Scale Neural Model (LSNM) simulator, which generated task-driven neural activity of the brain regions directly involved in the visual DMS task, and The Virtual Brain simulator (TVB) (Sanz Leon et al., 2013) to generate resting-state neural activity in the brain regions not involved in the task. Because the task-based brain nodes were embedded within resting-state brain ROIs, we expected that the neuroimaging activity in key connectome ROIs would differ between passive fixation (PF), passive viewing (PV), and task-based simulations. Here, we sought to

513 quantify those differences, first by comparing the pattern of functional connectivity across
514 conditions, then by using graph theoretical methods to quantify those differences.

515 Within the LSNM, connections and parameter choices closely follow those in the original
516 papers. Likewise, the connections and parameter choices among TVB nodes closely follow
517 those described by Sanz-Leon et al. (Sanz-Leon et al., 2015). There are two differences between
518 the simulations presented in this paper and the previous (Ulloa & Horwitz, 2016) paper: The
519 location of the FR units has been changed to PreSMA and the global coupling parameter has
520 been changed (after a parameter search procedure detailed below).

521 *a. Task-based model node placement in the TVB*

522 The connectome derived by Hagmann and colleagues (Hagmann et al., 2008) serves as a
523 source of neural noise to our task-based neural model. Such a connectome was obtained by
524 averaging the weighted network of five experimental subjects, where each one of the 998
525 nodes represents a region of interest covering a surface area of approximately 1.5 cm^2. The
526 connection weights among the nodes represent cortico-cortical connections given by white
527 matter connection density among the given nodes. As stated above, each node is represented
528 by a Wilson-Cowan population unit and thus each node is assumed to be comprised of one
529 excitatory and one inhibitory neural population. We implemented noise as an additive term to
530 the stochastic Euler integration scheme provided by the TVB software.

531

532 The locations of the four PFC nodes (FS, D1, D2, FR) require some comment. The
533 inclusion of these four neural populations in the original LSNMs was based on the

534 electrophysiological studies of Funahashi et al. (Funahashi, Bruce, & Goldman-Rakic, 1990) that
535 found in monkey PFC four distinct neuronal responses during a delayed response task: neurons
536 that (1) increased their activity when a stimulus was present (FS), (2) increased their activity
537 during the delay part of the task (D1), (3) increased their activity during both when a stimulus
538 was present and during the delay period (D2), and (4) increased their activity prior to making a
539 correct response (FR). It is not known if these neuronal types are found in separate anatomical
540 locations in PFC or are intermixed within the same brain area, although the latter is the more
541 likely case (except possibly for the FR population). In the original modeling studies of Tagamets
542 and Horwitz (Tagamets & Horwitz, 1998) and Husain et al. (Husain, Tagamets, Fromm, Braun, &
543 Horwitz, 2004), the functional neuroimaging data represented a single region that included all
544 four nodes. To illustrate the integrated synaptic activity and fMRI signal for each one of the
545 modules of the combined LSNM / TVB model separately, we have assigned a different spatial
546 location to each one of the four PFC sub-modules. We have used the Talairach coordinates of
547 the prefrontal cortex, based on (Haxby et al., 1991), for the submodule D1 and have designated
548 spatial locations in adjacent regions of interest for the FS and D2 submodules. The FR
549 submodule has been allocated to a spatial location determined by an fMRI study of working
550 memory in humans (Pessoa et al., 2002). See Table 1 for coordinate locations of each
551 module/submodule of the visual short-term memory nodes within the structural connectome.

552 *b. Simulating electrical activity and fMRI activity*

553 Electrical activities of each node in Hagmann's connectome (TVB equations)

554 Each one of the nodes in Hagmann's connectome is represented as a Wilson-Cowan
555 model of excitatory (E) and inhibitory (I) neuronal populations, as described in Sanz-Leon et al.
556 (Sanz-Leon et al., 2015):
557
558 $$\frac{dE_i}{dt} = \frac{1}{\tau_E}\left(-E_i + (k_E - r_E E_i) S_E \left[\alpha_E \left(c_{EE}E_i - c_{IE}I_i - \theta_E + \mathbf{\Gamma}(E_i, E, u_{ij})\right)\right]\right)$$
559
560 and
561
562 $$\frac{dI_i}{dt} = \frac{1}{\tau_I}\left(-I_i + (k_I - r_I I_i) S_I \left[\alpha_I \left(c_{EI}E_i - c_{II}I_i - \theta_I + \mathbf{\Gamma}(E_i, E, u_{ij})\right)\right]\right)$$
563
564 where S_E and S_I are sigmoid functions described by
565
566 $$S_a[f(\varphi)] = \frac{c}{1 + e^{(-a(f(\varphi_a)-b))}}$$
567
568 $c_{EE}, c_{EI}, c_{II}, c_{IE}$ are the connections within the single neuronal unit itself; note that, although
569 the original TVB Wilson-Cowan population model allows us to consider the influence of a local
570 neighborhood of neuronal populations, we have not used this feature in our current
571 simulations and have left that term out of the equations above; $\mathbf{\Gamma}(E_k, E, u_{kj})$ is the long-range
572 coupling function, defined as
573

$$\mathbf{\Gamma}(E_i, E, u_{ij}) = a_\Gamma \left(\sum_{j=1}^{l} u_{ij} E_j(t - \tau_{ij}) + \sum_{j=1}^{n} u_{ij} E_j(t - \tau_{ij}) \right)$$

where l is the number of nodes in the connectome and *n* is the number of LSNM units connected to a connectome node; a_Γ is a global coupling parameter (see Supplementary Table S1 and Table S2 for the definition and value of the parameters in the above equations).

Electrical activities of each LSNM unit

Each one of the submodules of the LSNM model contains 81 neuronal population units. Each one of those units is modeled as a Wilson-Cowan population of excitatory (E) and inhibitory (I) elements. The electrical activities of each one of those elements at time *t* is given by the following equations:

$$\frac{dE_i(t)}{dt} = \Delta \left(\frac{1}{1 + e^{-K_E[w_{EE}E_i(t) + w_{IE}I_i(t) + in_{iE}(t) - \phi_E + N(t)]}} \right) - \delta E_i(t)$$

and

$$\frac{dI_i(t)}{dt} = \Delta \left(\frac{1}{1 + e^{-K_I[w_{EI}E_i(t) + in_{iI}(t) - \phi_I + N(t)]}} \right) - \delta I_i(t)$$

where Δ is the rate of change, δ is the rate of decay, K_E, K_I are gain constants, ϕ_E, ϕ_I are input threshold values, $N(t)$ is a noise term, w_{EE}, w_{IE}, w_{EI} are the weights within a unit (the values of $\Delta, \delta, K, \tau, N$ are given in the Supplementary Table S3); $in_{iE}(t), in_{iI}(t)$ are the inputs coming from other brain regions at time t. $in_{iE}(t)$ is given by:

$$in_{iE}(t) = \sum_j w_{ji}^E E_j(t) + \sum_j w_{ji}^I I_j(t) + \sum_j c_{ji} z_{ji}^C C_j(t)$$

where w_{ji}^E and w_{ji}^I are the weights originating from excitatory (E) or inhibitory (I) unit *j* from another LSNM unit into the *i*th excitatory element, C_j is the connectome excitatory unit *j* with connections to the LSNM unit *i*, z_{ji}^C is the value of the anatomical connection weight from connectome unit *j* to LSNM unit *i*, and $c_{ji}$is a coupling term, which was obtained by using Python's Gaussian pseudo-random number generator (*random.gauss*), using $a_\Gamma/81$ as the mean value. The input coming into the *i*th inhibitory element, $in_{iI}(t)$, is given by:

$$in_{iI}(t) = \sum_k w_{ki}^E E_k(t) + \sum_k w_{ki}^I I_k(t)$$

where w_{ki}^E and w_{ki}^I are the weights originating from excitatory (E) or inhibitory (I) unit *k* from another LSNM unit into the *i*th inhibitory element. Note that there are no connections from the connectome to LSNM inhibitory units. See Supplementary Tables S4 and S5 for details. Note also that, whereas TVB simulator incorporates transmission delay among the connectome nodes, the LSNM nodes do not.

Integrated synaptic activity

Prior to computing fMRI BOLD activities we compute the synaptic activity, spatially integrated over each LSNM module (or connectome node) and temporally integrated over 50 milliseconds as described by (Horwitz & Tagamets, 1999)

615

616 $$rSYN = \sum_{t,i} IN_i(t)$$

617

618 where $IN_i(t)$ is the sum of absolute values of all inputs to both *E* and *I* elements of unit *i*, at

619 time *t*, and is given by:

620

621 $$IN_i(t) = w_{EE}E_i(t) + w_{EI}E_i(t) + |w_{IE}I_i(t)| + \sum_{k,i} w_{ki}E_k(t)$$

622

623 Note that the first three terms above are the synaptic weights from within unit *i* and the last

624 term is the sum of synaptic connections originating in all other LSNM units and connectome

625 nodes connected to unit *i*. Note also that, in our current scheme, there are no long-range

626 connections from inhibitory populations.

627

628 Generation of subjects and task performance of the LSNM model

629 We generated simulated subjects by creating several different sets of connection

630 weights among submodules of the LSNM visual network until we obtained the number of

631 desired subjects whose task performance was above 60 percent. However, the weights among

632 the nodes with the TVB connectome remained unchanged across subjects. The generation of

633 different connectome sets to simulate individual subjects is outside the scope of the current

634 paper but will be essential for future simulation studies investigating the effects of a behavioral

635 task on non-task brain nodes. Task performance was measured as the proportion of correct

636 responses over an experiment. A response in the response module (FR, described in the caption
637 to Fig. 1) was considered a correct response in each trial if at least 2 units had neuronal
638 electrical responses above a threshold of 0.7 during the response period. To create different
639 sets of weights that were different from the ideal subject, we multiplied feedforward
640 connections among modules in the LSNM visual model by a random proportion of between
641 0.95 and 1.
642
643 Equations for the forward fMRI BOLD model
644 We implemented the BOLD signal model described by (Stephan et al., 2007). We use the
645 output of the integrated synaptic activity above as the neural state equation to the
646 hemodynamic state equations below. The BOLD signal for each region of interest, *y(t)*, is
647 computed as follows:
648

649 $$y(t) = V_0\left(k_1(1-q(t)) + k_2\left(1-\frac{q(t)}{v(t)}\right) + k_3(1-v(t))\right).$$

650
651 where the coefficients k_1, k_2, k_3 are computed as:
652

653 $$k_1 = 4.3\vartheta_0 E_0 TE$$

654 $$k_2 = \varepsilon r_0 E_0 TE$$

655 $$k_3 = 1-\varepsilon$$

656

where V_0 is the resting venous blood volume fraction, q is the deoxyhemoglobin content, v is the venous blood volume, E_0 is the oxygen extraction fraction at rest, ε is the ratio of intra- and extravascular signals, and r_0 is the slope of the relation between the intravascular relaxation rate and oxygen saturation, ϑ_0 is the frequency offset at the outer surface of the magnetized vessel for fully deoxygenated blood at 3T, and TE is the echo time. The evolution of the venous blood volume v and deoxyhemoglobin content q is given by the balloon model hemodynamic state equations, as follows:

$$\tau_0 \frac{dv}{dt} = f(t) - v(t)^{1/\alpha}$$

$$\tau_0 \frac{dq}{dt} = f(t)\frac{1-(1-E_0)^{1/f}}{E_0} - v(t)^{1/\alpha}\frac{q(t)}{v(t)}$$

where τ_0 is the hemodynamics transit time, α represents the resistance of the venous balloon (vessel stiffness), and $f(t)$ is the blood inflow at time t and is given by

$$\frac{df}{dt} = s$$

where s is an exponentially decaying, vasodilatory signal given by

$$\frac{ds}{dt} = \epsilon x(t) - \frac{s(t)}{\tau_s} - \frac{(f(t)-1)}{\tau_f}$$

where $\epsilon$is the efficacy with which neuronal activity *x(t)* (i.e., integrated synaptic activity) causes an increase in signal, τ_s-is the time constant for signal decay, and τ_f-is the time constant for autoregulatory feedback from blood flow (Friston et al., 2000). See Supplementary Table S6 for the values of the above parameters. The simulated fMRI BOLD time series resulting from the above equations were low-pass filtered (<0.25Hz) and down-sampled every two seconds.

Resting State parameter exploration

We performed a global parameter exploration (for which we used exclusively the TVB simulator and the structural connectome with no task nodes) to obtain a reasonable match between empirical and model FC (Cabral et al., 2011). We obtained the empirical functional connectivity datasets from (Hagmann et al., 2008) which we used as a target for our simulated FC. Note that we used a low resolution (66 nodes) FC of matrices to perform the comparisons between empirical and resting state simulations (Honey et al., 2009): We transformed all correlation coefficients to Fisher's Z values and averaged the FC matrices across subjects within each condition. We then calculated low-resolution (66 ROIs) matrices (each ROI corresponding to a brain region in the Desikan-Killiany parcellation (Desikan et al., 2006) for each condition (Hagmann et al., 2008; Honey et al., 2009) by averaging FC coefficients within each one of the low-resolution ROIs (Hagmann et al., 2008) and converted back to correlation coefficients using an inverse Fisher's Z transformation. We systematically varied the global coupling parameter (a_Γ in the long-range coupling equation above) and the white matter conduction speed and conducted a 198-second resting state simulation for each parameter combination. We calculated a Pearson correlation coefficient between the model FC matrix (for each parameter

699 combination) and the empirical FC matrix. Then, we chose the parameter combination that
700 gave us the highest correlation value and used that combination for the PF, PV and DMS
701 simulations of our study. The global strength parameter range used was between 0.0042 and
702 0.15 with a step of 0.01. The conduction speed parameter range used was between 1 and 10
703 m/s with a step of 1. The best combination of parameters was (0.15, 3) which yielded a
704 correlation value between simulated and empirical FC of r=0.37. Note that absent structural
705 connections were removed from this correlation calculation as in (Honey et al., 2009), but not
706 in the rest of the paper.
707
708 **From RS to PF, PV, and DMS**
709 After finding an optimal match between empirical and simulated RS, we performed a simulation
710 of RS with stimulation in visual task nodes using only the TVB simulator (Sanz-Leon et al., 2015).
711 The correlation between RS FC and RS with stimulation FC was 0.90. Subsequently, we used a
712 blend of our LSNM simulator and TVB to simulated PF. The correlation between RS with
713 stimulation and PF was 0.9. As a last step, we performed a DMS simulation and compared it to
714 the PF simulation (correlation was 0.79). Thus, we used a TVB RS simulation (matched to
715 empirical RS) as a starting point for our PF and task-based simulations.
716
717 **Network construction**
718 The simulations were performed using the TVB simulator with the 998-node Hagmann
719 connectome and the LSNM visual short-term memory simulator described above. We isolated
720 the synaptic activity timeseries of connectome nodes from the task nodes' synaptic activity. We

721 used the Balloon model to estimate fMRI BOLD activation over each one of the 998 nodes, for
722 each condition, and for each subject separately. We calculated zero lag Pearson correlation
723 coefficients for each pair of the BOLD timeseries to obtain a FC matrix for each condition and
724 for each subject. We used the weighted FC matrices within each condition to construct graphs
725 where each one of the 998 ROIs corresponded to a graph node and the correlation coefficients
726 between each pair of ROIs corresponded to graph edges (Bolt, Nomi, et al., 2017; Di et al.,
727 2013). To keep the same number of edges across conditions, we thresholded the network
728 edges to a sparsity level of between 5% and 40% (Di et al., 2013) with a step size of 5%.
729
730 **Graph theory analysis**
731 A set of eight graph theoretical metrics (global efficiency, local efficiency, clustering coefficient,
732 characteristic path length, eigenvector centrality, betweenness centrality, participation
733 coefficient, and modularity) were calculated using the FC matrices for each of the conditions
734 using the Brain Connectivity Toolbox (Rubinov & Sporns, 2010) in Python, publicly available at
735 https://github.com/aestrivex/bctpy. We calculated graph metrics for each individual FC matrix,
736 for each condition and for each density threshold. Then we calculated the average and standard
737 deviation of each graph metric for each density threshold.
738 *Global efficiency* (Latora & Marchiori, 2001) measures "functional integration" (Rubinov &
739 Sporns, 2010) and indicates how well nodes are coupled through functional connections across
740 the entire brain. Global efficiency is calculated as the average inverse shortest path length
741 (Rubinov & Sporns, 2010). *Local efficiency* is the inverse of the average shortest path
742 connecting a given node to its neighbors (Lee et al., 2017). *Clustering coefficient* (Watts &

743 Strogatz, 1998) is a measure of "functional segregation" (Rubinov & Sporns, 2010). The
744 clustering coefficient of a network node is the proportion of the given node's neighbors that are
745 functionally connected to each other. Whole brain clustering coefficient is calculated as the
746 average of the clustering coefficients in a functional connectivity matrix (Rubinov & Sporns,
747 2010). *Characteristic path length* is the average shortest path length between all node pairs in a
748 network (Rubinov & Sporns, 2010). *Eigenvector centrality* is a measure of centrality that
749 considers degree of a given node and degree of that node's neighbors (Fornito, Zalesky, &
750 Bullmore, 2016 2016). Betweenness centrality is the fraction of shortest paths that cross a given
751 network node (Rubinov & Sporns, 2010). *Participation coefficient* is a measure of each node's
752 participation in a given set of network communities. We used a set of six network communities
753 for the participation coefficient calculation, as shown in Table S1 of (Hagmann et al., 2008),
754 Table S1. *Modularity* (Newman, 2004) is a metric of functional segregation and it detects
755 community structure in a network by dividing a functional connectivity matrix into sets of non-
756 overlapping modules and it measures how well a network can be divided into those modules
757 (Rubinov & Sporns, 2010).
758
759 **SUPPORTING INFORMATION**
760 Table S1. Parameters used in the Wilson-Cowan equation for each connectome within TVB.
761 Table S2. Parameters used for simulating the Hagmann connectome within the TVB simulator.
762 Table S3. Parameters used in the Wilson-Cowan unit model of each LSNM submodule.
763 Table S4. Connection patterns among submodules of the LSNM model.
764 Table S5. Connection weights among submodules in the prefrontal cortex regions of LSNM.

765 Table S6. Parameters used for the Balloon model of hemodynamic response.

766

767 **ACKNOWLEDGEMENTS**

768 This research was funded by the Division of Intramural Research of the National Institute on
769 Deafness and Other Communication Disorders. We thank Olaf Sporns and Chris Honey for
770 sharing the functional and structural connectivity data sets from their empirical studies used in
771 the present paper. We thank Paul Corbitt for useful discussions related to the simulation code
772 used for our analysis and the parameters used for converting synaptic activity to fMRI BOLD
773 time-series. We thank Marmaduke Woodman for helping us navigate technical aspects of the
774 TVB simulator.

775

776 **REFERENCES**

777 Adams, R. A., Shipp, S., & Friston, K. J. (2013). Predictions not commands: active inference in
778 the motor system. *Brain Struct Funct, 218*(3), 611-643. doi:10.1007/s00429-012-0475-5
779 Bastian, M., Heymann, S., & Jacomy, M. (2009). Gephi: an open source software for exploring
780 and manipulating networks. *International AAAI conference on weblogs and social media*,
781 361-362.
782 Benjamin, C., Lieberman, D. A., Chang, M., Ofen, N., Whitfield-Gabrieli, S., Gabrieli, J. D., &
783 Gaab, N. (2010). The influence of rest period instructions on the default mode network.
784 *Front Hum Neurosci, 4*, 218. doi:10.3389/fnhum.2010.00218

785 Biswal, B., Yetkin, F. Z., Haughton, V. M., & Hyde, J. S. (1995). Functional connectivity in the
786 motor cortex of resting human brain using echo-planar MRI. *Magn Reson Med, 34*(4),
787 537-541.
788 Blondel, V. D., Guillaume, J.-L., Lambiotte, R., & Lefebvre, E. (2008). Fast unfolding of
789 communities in large networks. *J, Stat. Mech.*(2008), P10008. doi:DOI: 10.1088/1742-
790 5468/2008/10/P10008
791 Bluhm, R. L., Clark, C. R., McFarlane, A. C., Moores, K. A., Shaw, M. E., & Lanius, R. A. (2011).
792 Default network connectivity during a working memory task. *Hum Brain Mapp, 32*(7),
793 1029-1035. doi:10.1002/hbm.21090
794 Bolt, T., Anderson, M. L., & Uddin, L. Q. (2017). Beyond the evoked/intrinsic neural process
795 dichotomy. *Network Neuroscience, 0*(0), 1-22. doi:10.1162/NETN_a_00028
796 Bolt, T., Nomi, J. S., Rubinov, M., & Uddin, L. Q. (2017). Correspondence between evoked and
797 intrinsic functional brain network configurations. *Hum Brain Mapp*.
798 doi:10.1002/hbm.23500
799 Branco, P., Seixas, D., Deprez, S., Kovacs, S., Peeters, R., Castro, S. L., & Sunaert, S. (2016).
800 Resting-State Functional Magnetic Resonance Imaging for Language Preoperative
801 Planning. *Front Hum Neurosci, 10*, 11. doi:10.3389/fnhum.2016.00011
802 Buckner, R. L., Sepulcre, J., Talukdar, T., Krienen, F. M., Liu, H., Hedden, T., . . . Johnson, K. A.
803 (2009). Cortical hubs revealed by intrinsic functional connectivity: mapping, assessment
804 of stability, and relation to Alzheimer's disease. *J Neurosci, 29*(6), 1860-1873.
805 doi:10.1523/JNEUROSCI.5062-08.2009

806 Cabral, J., Hugues, E., Sporns, O., & Deco, G. (2011). Role of local network oscillations in resting-
807 state functional connectivity. [Yes-HL]. *Neuroimage, 57*(1), 130-139. doi:S1053-
808 8119(11)00388-0 [pii]
809 10.1016/j.neuroimage.2011.04.010
810 Chaudhuri, R., Knoblauch, K., Gariel, M. A., Kennedy, H., & Wang, X. J. (2015). A Large-Scale
811 Circuit Mechanism for Hierarchical Dynamical Processing in the Primate Cortex. *Neuron,*
812 *88*(2), 419-431. doi:10.1016/j.neuron.2015.09.008
813 Cohen, J. R., & D'Esposito, M. (2016). The Segregation and Integration of Distinct Brain
814 Networks and Their Relationship to Cognition. *J Neurosci, 36*(48), 12083-12094.
815 doi:10.1523/JNEUROSCI.2965-15.2016
816 Cole, M. W., Bassett, D. S., Power, J. D., Braver, T. S., & Petersen, S. E. (2014). Intrinsic and task-
817 evoked network architectures of the human brain. *Neuron, 83*(1), 238-251.
818 doi:10.1016/j.neuron.2014.05.014
819 Cole, M. W., Ito, T., Bassett, D. S., & Schultz, D. H. (2016). Activity flow over resting-state
820 networks shapes cognitive task activations. *Nat Neurosci, 19*(12), 1718-1726.
821 doi:10.1038/nn.4406
822 DeSalvo, M. N., Douw, L., Takaya, S., Liu, H., & Stufflebeam, S. M. (2014). Task-dependent
823 reorganization of functional connectivity networks during visual semantic decision
824 making. *Brain Behav, 4*(6), 877-885. doi:10.1002/brb3.286
825 Desikan, R. S., Segonne, F., Fischl, B., Quinn, B. T., Dickerson, B. C., Blacker, D., . . . Killiany, R. J.
826 (2006). An automated labeling system for subdividing the human cerebral cortex on MRI

827 scans into gyral based regions of interest. *Neuroimage, 31*(3), 968-980.
828 doi:10.1016/j.neuroimage.2006.01.021
829 Di, X., Gohel, S., Kim, E. H., & Biswal, B. B. (2013). Task vs. rest-different network configurations
830 between the coactivation and the resting-state brain networks. *Front Hum Neurosci, 7*,
831 493. doi:10.3389/fnhum.2013.00493
832 Fornito, A., Zalesky, A., & Bullmore, E. T. (2016). *Fundamental of brain network analysis*.
833 Amsterdam ; Boston: Elsevier/Academic Press.
834 Fox, M. D., Corbetta, M., Snyder, A. Z., Vincent, J. L., & Raichle, M. E. (2006). Spontaneous
835 neuronal activity distinguishes human dorsal and ventral attention systems. *Proc Natl*
836 *Acad Sci U S A, 103*(26), 10046-10051. doi:10.1073/pnas.0604187103
837 Friston, K. J., Mechelli, A., Turner, R., & Price, C. J. (2000). Nonlinear responses in fMRI: the
838 Balloon model, Volterra kernels, and other hemodynamics. *Neuroimage, 12*(4), 466-477.
839 doi:10.1006/nimg.2000.0630
840 Fuertinger, S., Horwitz, B., & Simonyan, K. (2015). The Functional Connectome of Speech
841 Control. *PLoS Biol, 13*(7), e1002209. doi:10.1371/journal.pbio.1002209
842 Funahashi, S., Bruce, C. J., & Goldman-Rakic, P. S. (1990). Visuospatial coding in primate
843 prefrontal neurons revealed by oculomotor paradigms. *J Neurophysiol, 63*(4), 814-831.
844 doi:10.1152/jn.1990.63.4.814
845 Ghosh, A., Rho, Y., McIntosh, A. R., Kotter, R., & Jirsa, V. K. (2008). Noise during rest enables the
846 exploration of the brain's dynamic repertoire. *PLoS Comput Biol, 4*(10), e1000196.
847 doi:10.1371/journal.pcbi.1000196

848 Gilson, M., Moreno-Bote, R., Ponce-Alvarez, A., Ritter, P., & Deco, G. (2016). Estimation of
849 Directed Effective Connectivity from fMRI Functional Connectivity Hints at Asymmetries
850 of Cortical Connectome. *PLoS Comput Biol, 12*(3), e1004762.
851 doi:10.1371/journal.pcbi.1004762
852 Greicius, M. D., Krasnow, B., Reiss, A. L., & Menon, V. (2003). Functional connectivity in the
853 resting brain: a network analysis of the default mode hypothesis. *Proc Natl Acad Sci U S*
854 *A, 100*(1), 253-258. doi:10.1073/pnas.0135058100
855 Hagmann, P., Cammoun, L., Gigandet, X., Meuli, R., Honey, C. J., Wedeen, V. J., & Sporns, O.
856 (2008). Mapping the structural core of human cerebral cortex. *PLoS Biol, 6*(7), e159.
857 doi:10.1371/journal.pbio.0060159
858 Hansen, E. C., Battaglia, D., Spiegler, A., Deco, G., & Jirsa, V. K. (2015). Functional connectivity
859 dynamics: modeling the switching behavior of the resting state. *Neuroimage, 105*, 525-
860 535. doi:10.1016/j.neuroimage.2014.11.001
861 Havlicek, M., Roebroeck, A., Friston, K., Gardumi, A., Ivanov, D., & Uludag, K. (2015).
862 Physiologically informed dynamic causal modeling of fMRI data. *Neuroimage, 122*, 355-
863 372. doi:10.1016/j.neuroimage.2015.07.078
864 Haxby, J. V., Grady, C. L., Horwitz, B., Ungerleider, L. G., Mishkin, M., Carson, R. E., . . . Rapoport,
865 S. I. (1991). Dissociation of object and spatial visual processing pathways in human
866 extrastriate cortex. *Proc. Natl. Acad. Sci. USA, 88*, 1621-1625.
867 Haxby, J. V., Ungerleider, L. G., Horwitz, B., Rapoport, S. I., & Grady, C. L. (1995). Hemispheric
868 differences in neural systems for face working memory: A PET-rCBF study. *Human Brain*
869 *Mapp., 3*(2), 68-82. doi:DOI 10.1002/hbm.460030204

870 Heinzle, J., Koopmans, P. J., den Ouden, H. E., Raman, S., & Stephan, K. E. (2016). A
871 hemodynamic model for layered BOLD signals. *Neuroimage, 125*, 556-570.
872 doi:10.1016/j.neuroimage.2015.10.025
873 Honey, C. J., Sporns, O., Cammoun, L., Gigandet, X., Thiran, J. P., Meuli, R., & Hagmann, P.
874 (2009). Predicting human resting-state functional connectivity from structural
875 connectivity. *Proc Natl Acad Sci U S A, 106*(6), 2035-2040. doi:10.1073/pnas.0811168106
876 Horwitz, B., & Tagamets, M.-A. (1999). Predicting human functional maps with neural net
877 modeling. *Human Brain Mapp., 8*, 137-142.
878 Horwitz, B., Warner, B., Fitzer, J., Tagamets, M. A., Husain, F. T., & Long, T. W. (2005).
879 Investigating the neural basis for functional and effective connectivity. Application to
880 fMRI. *Philos Trans R Soc Lond B Biol Sci, 360*(1457), 1093-1108.
881 doi:10.1098/rstb.2005.1647
882 Husain, F. T., Tagamets, M. A., Fromm, S. J., Braun, A. R., & Horwitz, B. (2004). Relating neuronal
883 dynamics for auditory object processing to neuroimaging activity: a computational
884 modeling and an fMRI study. *Neuroimage, 21*(4), 1701-1720.
885 doi:10.1016/j.neuroimage.2003.11.012
886 Jbabdi, S., Sotiropoulos, S. N., Haber, S. N., Van Essen, D. C., & Behrens, T. E. (2015). Measuring
887 macroscopic brain connections in vivo. *Nat Neurosci, 18*(11), 1546-1555.
888 doi:10.1038/nn.4134
889 Krienen, F. M., Yeo, B. T., & Buckner, R. L. (2014). Reconfigurable task-dependent functional
890 coupling modes cluster around a core functional architecture. *Philos Trans R Soc Lond B*
891 *Biol Sci, 369*(1653). doi:10.1098/rstb.2013.0526

892 Latora, V., & Marchiori, M. (2001). Efficient behavior of small-world networks. *Phys Rev Lett,*
893 *87*(19), 198701. doi:10.1103/PhysRevLett.87.198701
894 Lee, W. H., Bullmore, E., & Frangou, S. (2017). Quantitative evaluation of simulated functional
895 brain networks in graph theoretical analysis. *Neuroimage, 146*, 724-733.
896 doi:10.1016/j.neuroimage.2016.08.050
897 Liu, H., Buckner, R. L., Talukdar, T., Tanaka, N., Madsen, J. R., & Stufflebeam, S. M. (2009). Task-
898 free presurgical mapping using functional magnetic resonance imaging intrinsic activity.
899 *J Neurosurg, 111*(4), 746-754. doi:10.3171/2008.10.JNS08846
900 Maier-Hein, K. H., Neher, P. F., Houde, J. C., Cote, M. A., Garyfallidis, E., Zhong, J., . . .
901 Descoteaux, M. (2017). The challenge of mapping the human connectome based on
902 diffusion tractography. *Nat Commun, 8*(1), 1349. doi:10.1038/s41467-017-01285-x
903 McIntosh, A. R., Grady, C. L., Ungerleider, L. G., Haxby, J. V., Rapoport, S. I., & Horwitz, B.
904 (1994). Network analysis of cortical visual pathways mapped with PET. *J. Neurosci., 14*,
905 655-666.
906 Meunier, D., Fonlupt, P., Saive, A. L., Plailly, J., Ravel, N., & Royet, J. P. (2014). Modular structure
907 of functional networks in olfactory memory. *Neuroimage, 95*, 264-275.
908 doi:10.1016/j.neuroimage.2014.03.041
909 Moussa, M. N., Vechlekar, C. D., Burdette, J. H., Steen, M. R., Hugenschmidt, C. E., & Laurienti,
910 P. J. (2011). Changes in cognitive state alter human functional brain networks. *Front*
911 *Hum Neurosci, 5*, 83. doi:10.3389/fnhum.2011.00083
912 Newman, M. E. (2004). Fast algorithm for detecting community structure in networks. *Phys Rev*
913 *E Stat Nonlin Soft Matter Phys, 69*(6 Pt 2), 066133. doi:10.1103/PhysRevE.69.066133

914 Obata, T., Liu, T. T., Miller, K. L., Luh, W.-M., Wong, E. C., Frank, L. R., & Buxton, R. B. (2004).
915 Discrepancies between BOLD and flow dynamics in primary and supplementary motor
916 areas: application of the balloon model to the interpretation of BOLD transients.
917 *Neuroimage, 21*(1), 144-153. doi:10.1016/j.neuroimage.2003.08.040
918 Pessoa, L., Gutierrez, E., Bandettini, P., & Ungerleider, L. (2002). Neural correlates of visual
919 working memory: fMRI amplitude predicts task performance. *Neuron, 35*(5), 975-987.
920 Petit, L., Courtney, S. M., Ungerleider, L. G., & Haxby, J. V. (1998). Sustained activity in the
921 medial wall during working memory delays. *J Neurosci, 18*(22), 9429-9437.
922 Ponce-Alvarez, A., He, B. J., Hagmann, P., & Deco, G. (2015). Task-Driven Activity Reduces the
923 Cortical Activity Space of the Brain: Experiment and Whole-Brain Modeling. [Yes-HL].
924 *PLoS Comput Biol, 11*(8), e1004445. doi:10.1371/journal.pcbi.1004445
925 Roy, D., Sigala, R., Breakspear, M., McIntosh, A. R., Jirsa, V. K., Deco, G., & Ritter, P. (2014).
926 Using the virtual brain to reveal the role of oscillations and plasticity in shaping brain's
927 dynamical landscape. *Brain Connect, 4*(10), 791-811. doi:10.1089/brain.2014.0252
928 Rubinov, M., & Sporns, O. (2010). Complex network measures of brain connectivity: uses and
929 interpretations. *Neuroimage, 52*(3), 1059-1069. doi:10.1016/j.neuroimage.2009.10.003
930 Sanz Leon, P., Knock, S. A., Woodman, M. M., Domide, L., Mersmann, J., McIntosh, A. R., & Jirsa,
931 V. (2013). The Virtual Brain: a simulator of primate brain network dynamics. [Yes-HL].
932 *Front Neuroinform, 7*, 10. doi:10.3389/fninf.2013.00010
933 Sanz-Leon, P., Knock, S. A., Spiegler, A., & Jirsa, V. K. (2015). Mathematical framework for large-
934 scale brain network modeling in The Virtual Brain. *Neuroimage, 111*, 385-430.
935 doi:10.1016/j.neuroimage.2015.01.002

936 Smith, S. M., Fox, P. T., Miller, K. L., Glahn, D. C., Fox, P. M., Mackay, C. E., . . . Beckmann, C. F.
937 (2009). Correspondence of the brain's functional architecture during activation and rest.
938 *Proc Natl Acad Sci U S A, 106*(31), 13040-13045. doi:10.1073/pnas.0905267106
939 Stephan, K. E., Marshall, J. C., Penny, W. D., Friston, K. J., & Fink, G. R. (2007). Interhemispheric
940 integration of visual processing during task-driven lateralization. *J Neurosci, 27*(13),
941 3512-3522. doi:10.1523/JNEUROSCI.4766-06.2007
942 Stevens, A. A., Tappon, S. C., Garg, A., & Fair, D. A. (2012). Functional brain network modularity
943 captures inter- and intra-individual variation in working memory capacity. *PLoS One,*
944 *7*(1), e30468. doi:10.1371/journal.pone.0030468
945 Tagamets, M.-A., & Horwitz, B. (1998). Integrating electrophysiological and anatomical
946 experimental data to create a large-scale model that simulates a delayed match-to-
947 sample human brain imaging study. *Cereb. Cortex, 8*, 310-320.
948 Tomasi, D., Wang, R., Wang, G. J., & Volkow, N. D. (2014). Functional connectivity and brain
949 activation: a synergistic approach. *Cereb Cortex, 24*(10), 2619-2629.
950 doi:10.1093/cercor/bht119
951 Tommasin, S., Mascali, D., Gili, T., Assan, I. E., Moraschi, M., Fratini, M., . . . Giove, F. (2017).
952 Task-Related Modulations of BOLD Low-Frequency Fluctuations within the Default
953 Mode Network. *Front Phys, 5*. doi:10.3389/fphy.2017.00031
954 Ulloa, A., & Horwitz, B. (2016). Embedding Task-Based Neural Models into a Connectome-Based
955 Model of the Cerebral Cortex. *Front Neuroinform, 10*, 32. doi:10.3389/fninf.2016.00032

956 Ungerleider, L. G., & Mishkin, M. (1982). Two cortical visual systems. In D. J. Ingle, M. A.
957 Goodale, & R. J. W. Mansfield (Eds.), *Analysis of Visual Behavior* (pp. 549-586).
958 Cambridge: MIT Press.
959 Van Dijk, K. R., Hedden, T., Venkataraman, A., Evans, K. C., Lazar, S. W., & Buckner, R. L. (2010).
960 Intrinsic functional connectivity as a tool for human connectomics: theory, properties,
961 and optimization. *J Neurophysiol, 103*(1), 297-321. doi:10.1152/jn.00783.2009
962 Vatansever, D., Menon, D. K., Manktelow, A. E., Sahakian, B. J., & Stamatakis, E. A. (2015).
963 Default mode network connectivity during task execution. *Neuroimage, 122*, 96-104.
964 doi:10.1016/j.neuroimage.2015.07.053
965 Waites, A. B., Stanislavsky, A., Abbott, D. F., & Jackson, G. D. (2005). Effect of prior cognitive
966 state on resting state networks measured with functional connectivity. *Hum Brain*
967 *Mapp, 24*(1), 59-68. doi:10.1002/hbm.20069
968 Watts, D. J., & Strogatz, S. H. (1998). Collective dynamics of 'small-world' networks. *Nature,*
969 *393*(6684), 440-442. doi:10.1038/30918
970 Wen, X., Zhang, D., Liang, B., Zhang, R., Wang, Z., Wang, J., . . . Huang, R. (2015).
971 Reconfiguration of the Brain Functional Network Associated with Visual Task Demands.
972 *PLoS One, 10*(7), e0132518. doi:10.1371/journal.pone.0132518
973 Wilson, H. R., & Cowan, J. D. (1972). Excitatory and inhibitory interactions in localized
974 populations of model neurons. *Biophys. J., 12*, 1-24.
975 Yan, C., Liu, D., He, Y., Zou, Q., Zhu, C., Zuo, X., . . . Zang, Y. (2009). Spontaneous brain activity in
976 the default mode network is sensitive to different resting-state conditions with limited
977 cognitive load. *PLoS One, 4*(5), e5743. doi:10.1371/journal.pone.0005743

978 Yeo, B. T., Krienen, F. M., Sepulcre, J., Sabuncu, M. R., Lashkari, D., Hollinshead, M., . . . Buckner,
979 R. L. (2011). The organization of the human cerebral cortex estimated by intrinsic
980 functional connectivity. *J Neurophysiol, 106*(3), 1125-1165. doi:10.1152/jn.00338.2011
981 Yue, Q., Martin, R. C., Fischer-Baum, S., Ramos-Nunez, A. I., Ye, F., & Deem, M. W. (2017). Brain
982 Modularity Mediates the Relation between Task Complexity and Performance. *J Cogn*
983 *Neurosci, 29*(9), 1532-1546. doi:10.1162/jocn_a_01142
984
985

Table 1. Hypothesized locations, in Talairach coordinates, of visual LSNM modules, along with the closest node in the Hagmann et al. connectome. Note that the locations of FS and D2 are not explicitly known (see text) and were chosen only to demonstrate validity of the method.

Visual submodule	Talairach location	Source	Host connectome node
V1/V2	(18, -88, 8)	(Haxby, Ungerleider, Horwitz, Rapoport, & Grady, 1995)	(14, -86, 7)
V4	(30, -72, -12)	(Haxby et al., 1995)	(33, -70, -7)
IT	(28, -36, -8)	(Haxby et al., 1995)	(31, -39, -6)
FS	Location selected for illustrative purposes		(47, 19, 9)
D1	(42, 26, 20)	(Haxby et al., 1995)	(43, 29, 21)
D2	Location selected for illustrative purposes		(42, 39, 2)
FR	(1, 7, 48)	(Pessoa et al., 2002)	(8, 6, 50)

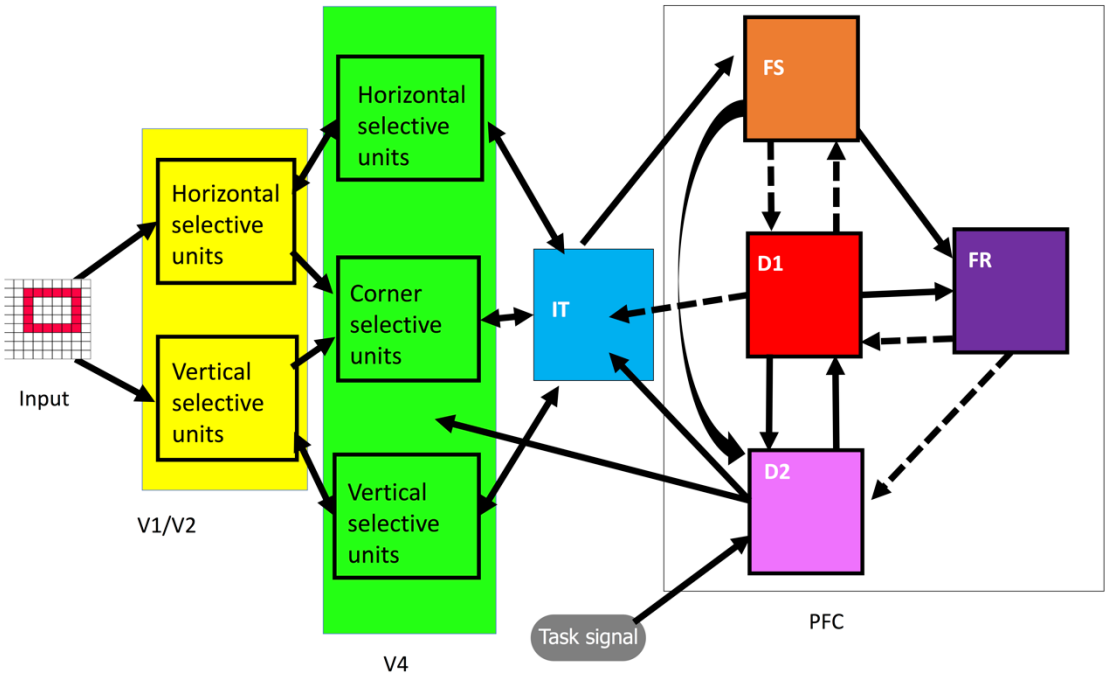

Figure 1. Visual short-term memory model consisted of interconnected neural populations that represent primary and secondary visual (V1/V2, V4), inferotemporal (IT), and prefrontal cortex (PFC). Each one of the sub-modules (shown above as squares) within a given brain module is modeled with 81 (9x9) modified Wilson-Cowan neuronal population units. Solid arrows represent Excitatory to Excitatory connections and dashed arrows represent Excitatory to Inhibitory connections. Adapted from (Horwitz et al., 2005).

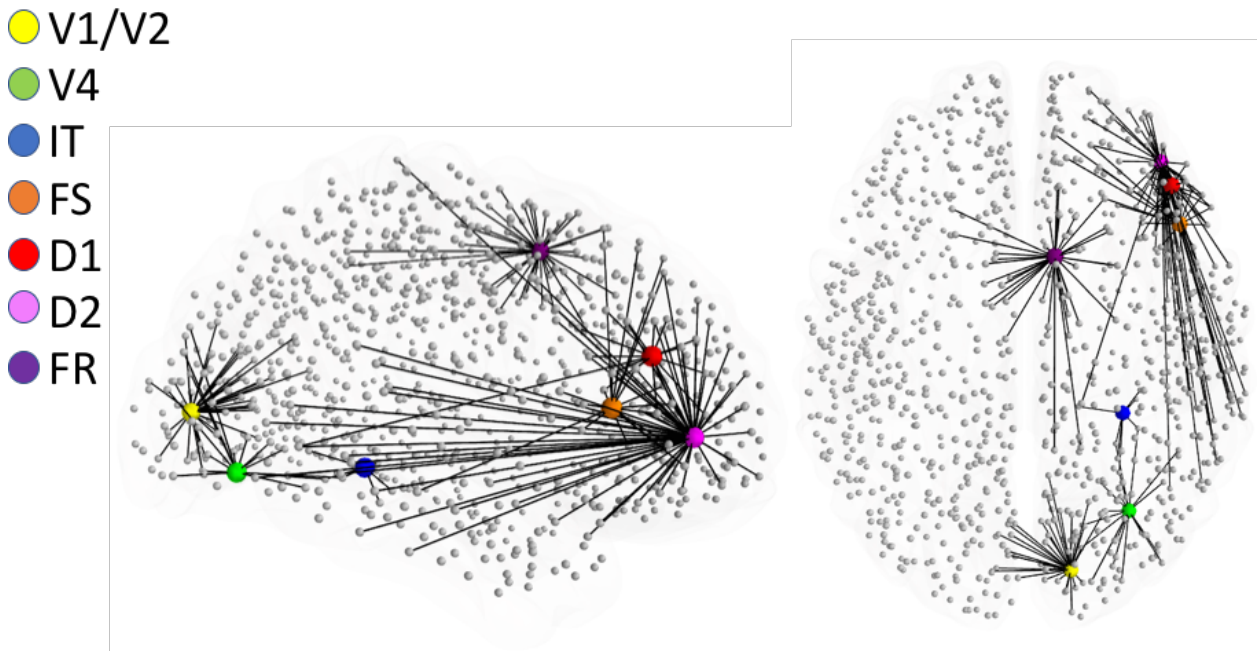

Figure 2. Graphical representation of the location where each of the visual short-term memory nodes was embedded within Hagmann's connectome (Hagmann et al., 2008). Also shown are direct anatomical connections to connectome nodes from each one of the embedded LSNM nodes.

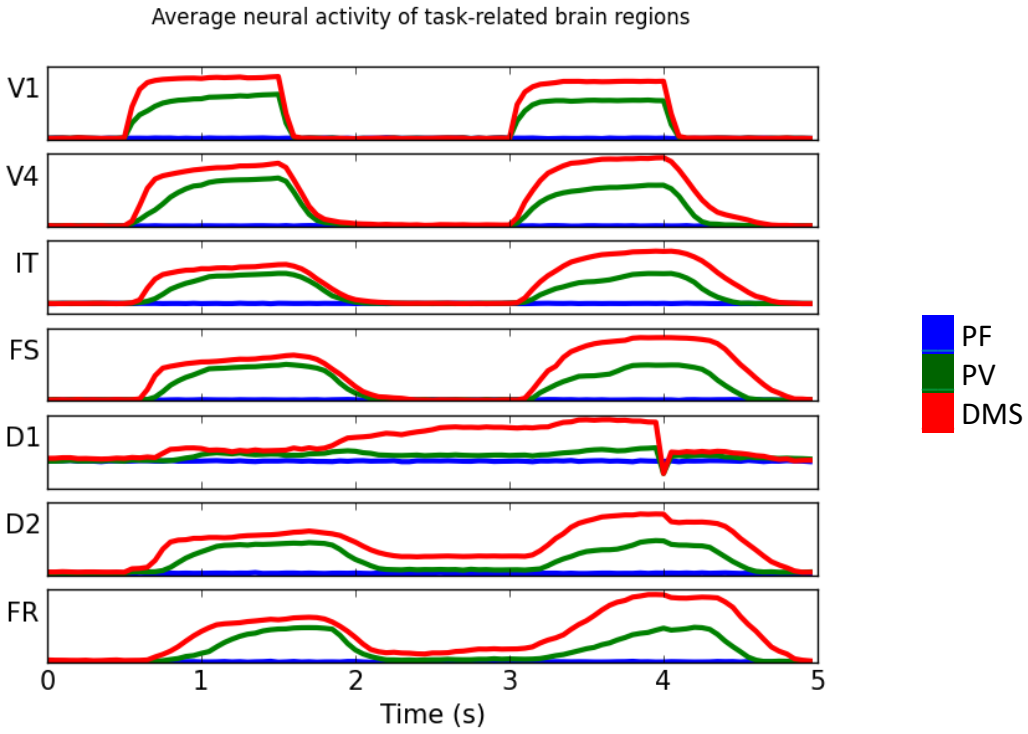

Figure 3. Typical electrical and in neuronal populations of task-related brain regions during one trail of each of the simulated conditions. Key: PF (blue line), PV (green line), DMS (red line). What is shown is the average across all cortical columns in a brain region.

1013

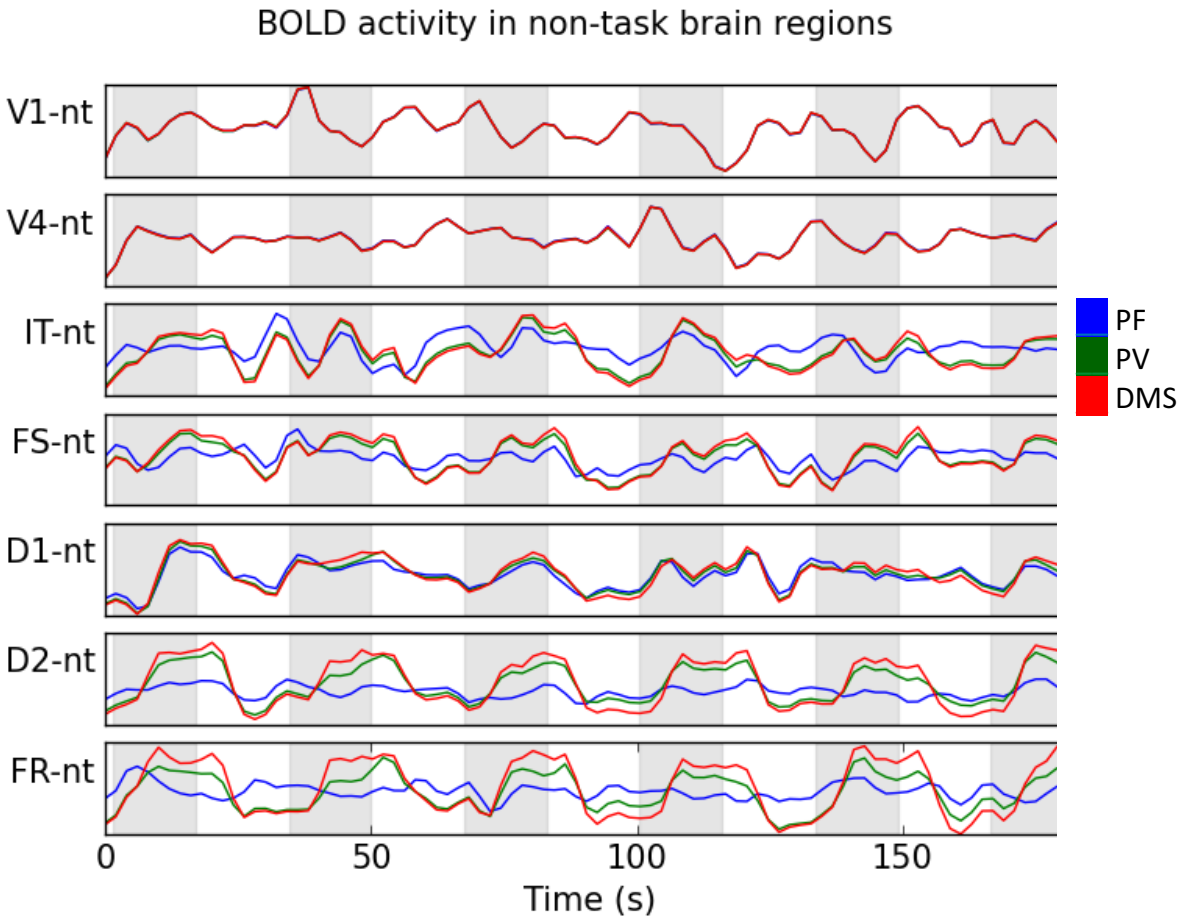

1014

1015 Figure 4. Average BOLD signal of non-task brain regions with direct connections to task related
1016 brain regions. A complete trial corresponding to 91 scans is shown above. for the PV and DMS
1017 conditions, each experiment above contains 6 task blocks (shaded regions) interspersed with
1018 rest blocks.

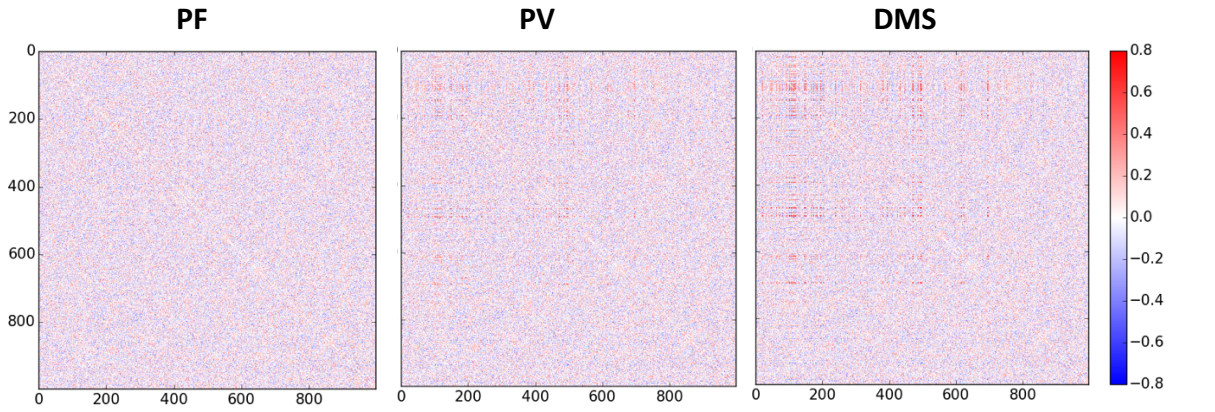

(A)

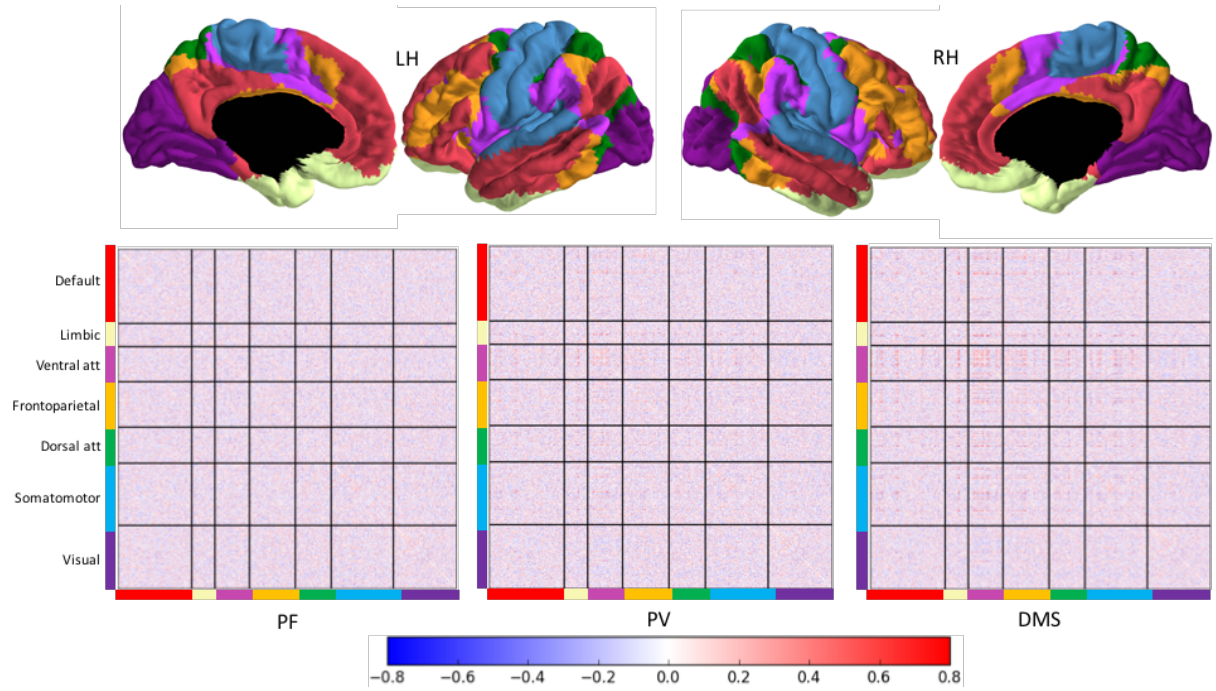

(B)

Figure 5. Representative correlation-based functional connectivity matrices for the three conditions simulated. Subject 12 is shown above. (A) The nodes in each matrix are arranged using the standard connectome files in (Hagmann et al., 2008). (B) Nodes in the matrix have been rearranged to match Yeo et al (Yeo et al., 2011) parcellation (7 modules). Brain parcellation was displayed using Freesurfer.

1033

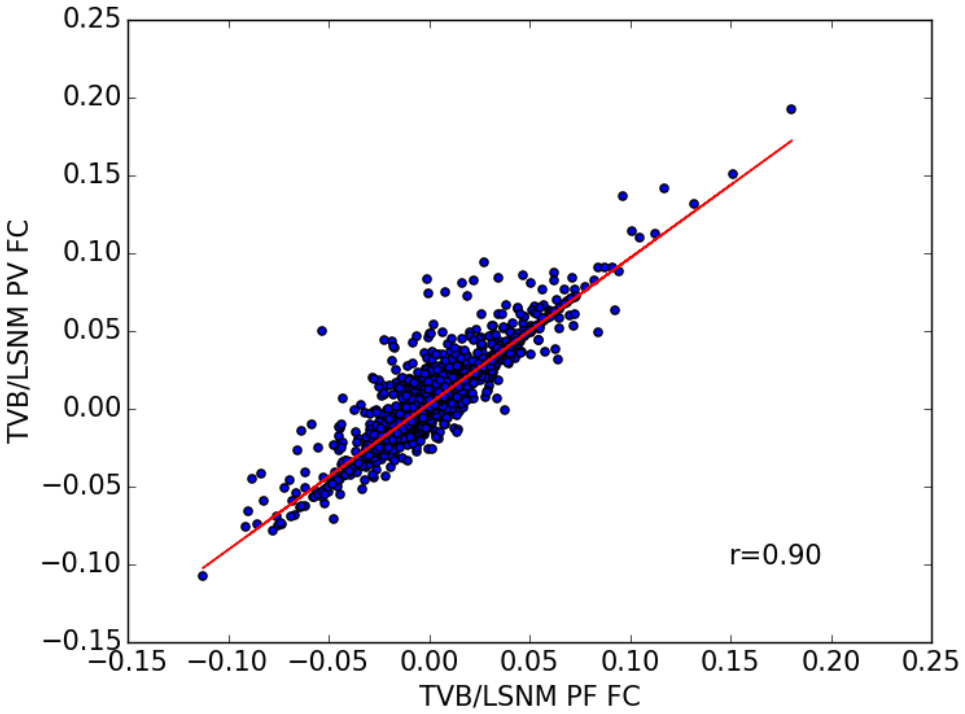

1034

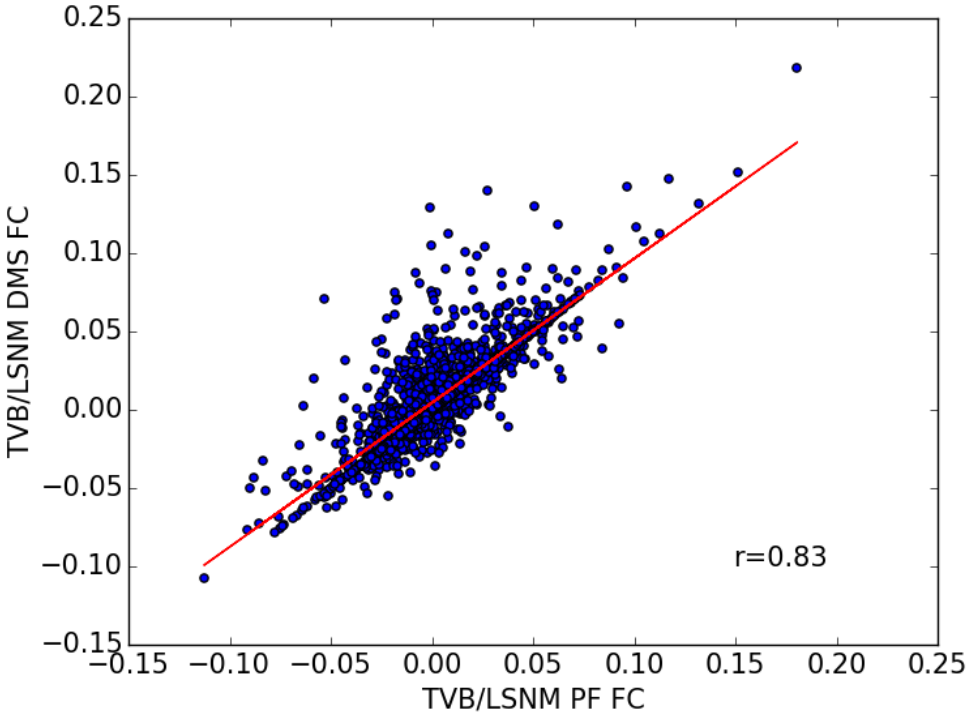

1035
1036

1037 **Figure 6.** Correlation between PF and PV and between PF and DMS weighted functional
1038 connectivity matrices.

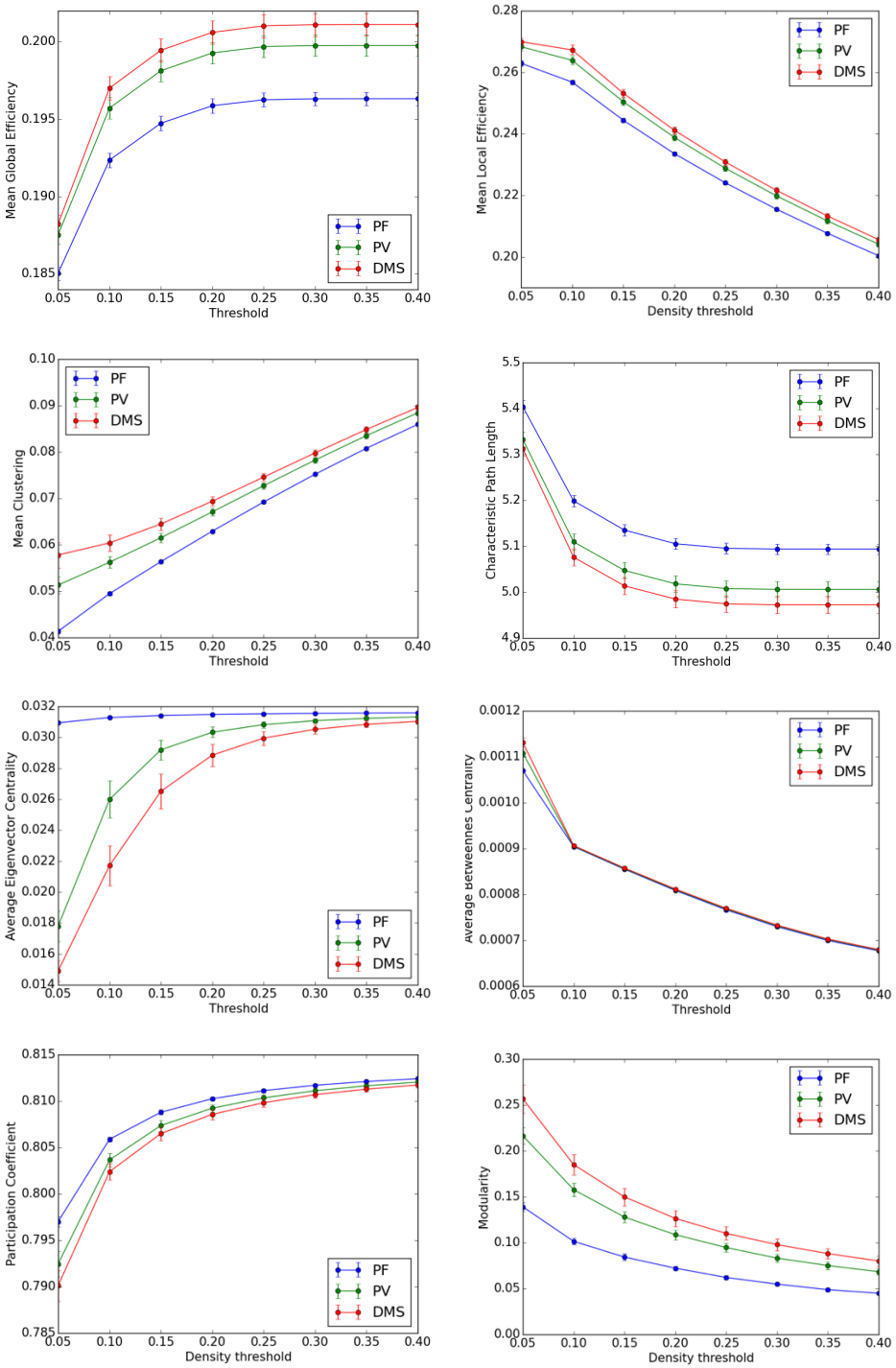

Figure 7. Mean graph theoretical metrics for each condition and for a range of network densities (5 to 40%). Error bars correspond to standard deviation.

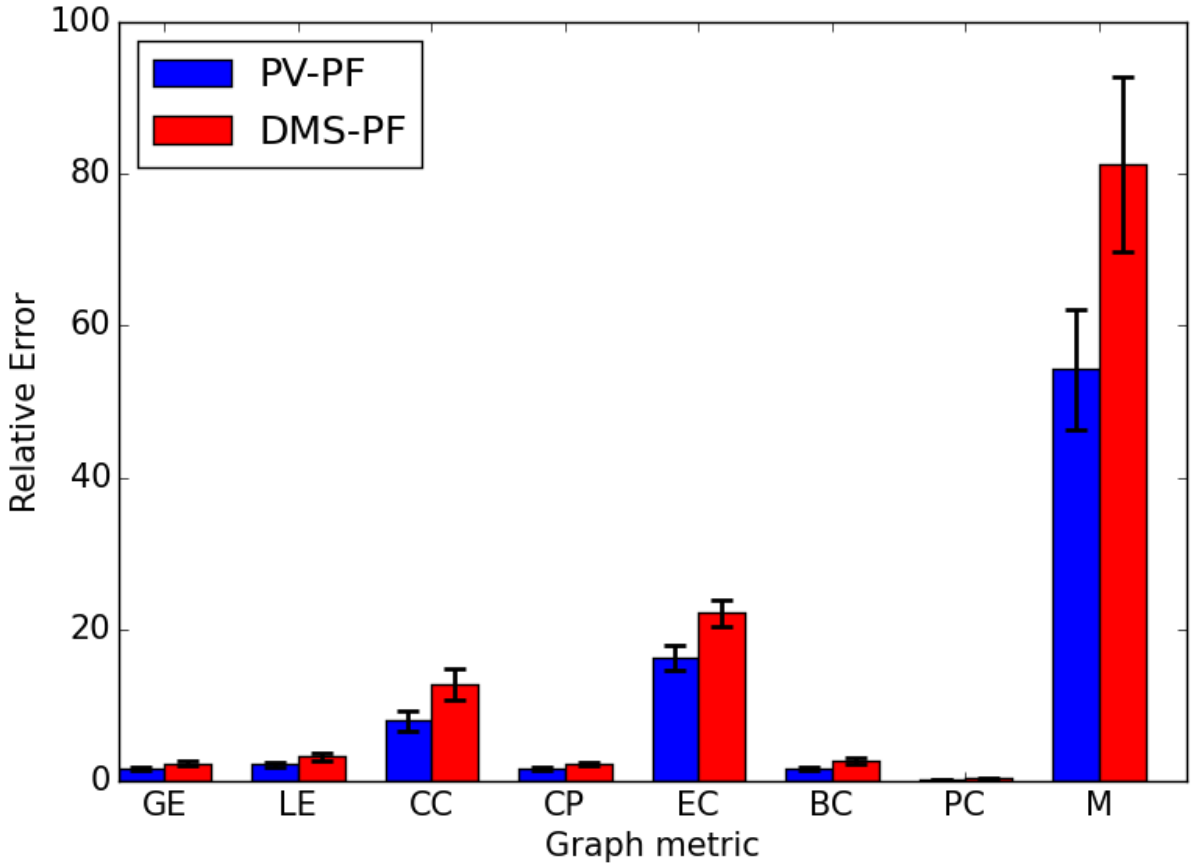

Figure 8. Relative difference between PF and PV and between PF and DMS for each one of the graph metrics in Figure 7. Error bars correspond to standard deviation.

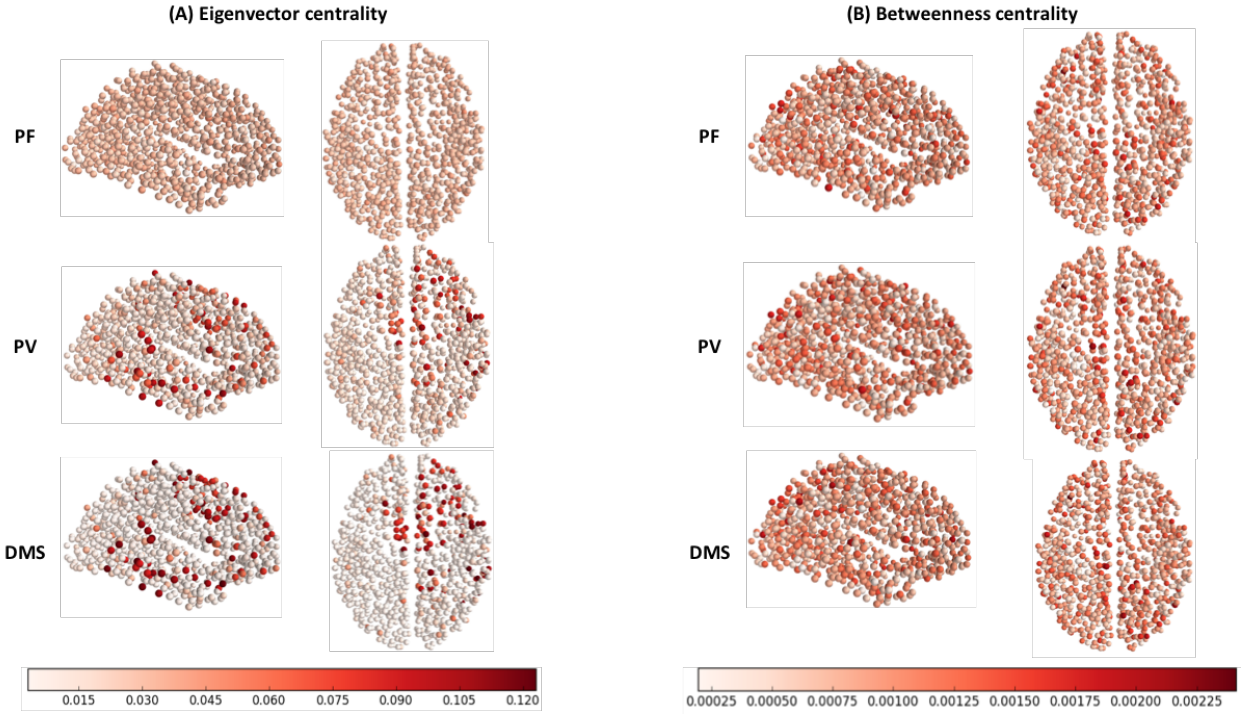

Figure 9. Eigenvector centrality (A) and betweenness centrality (B) depicted on a node-by-node basis on sagittal (left) and axial (right) views of the brain. The density threshold used for the depiction above was 10%.

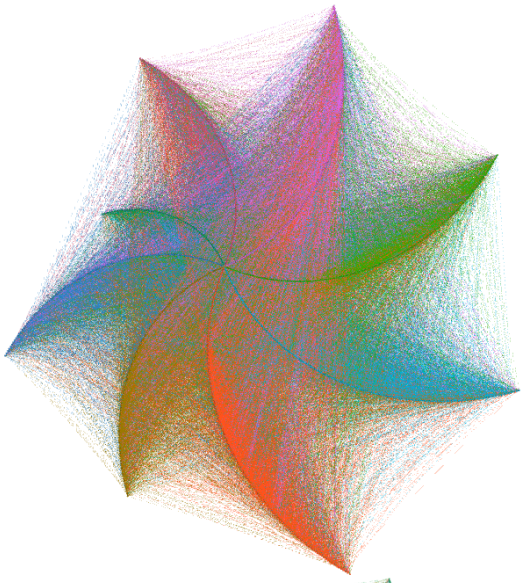

(A) PF
[8 modules]

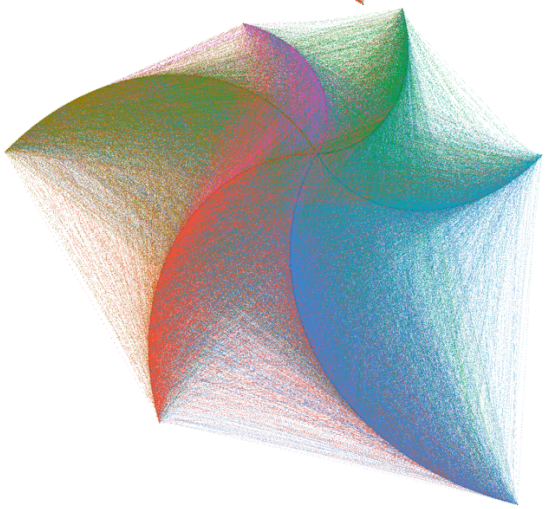

(B) PV
[6 modules]

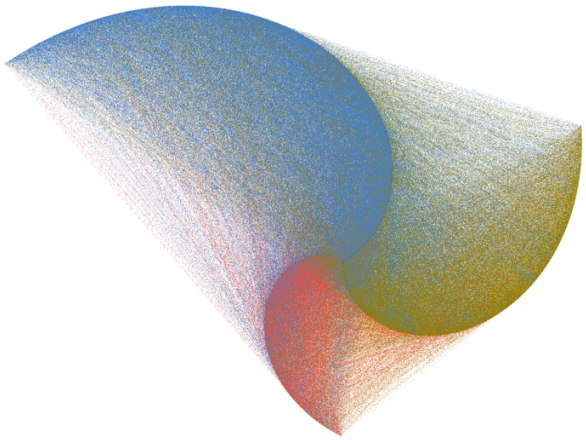

(C) DMS
[3 modules]

Figure 10. Modular structure of functional connectivity between non-task nodes in conditions (A) PF, (B) PV, and (C) DMS. The graphs used unweighted, undirected functional connectivity matrices at a density threshold of 10%. These graphs were rendered using the radial axis layout of Gephi (Bastian et al., 2009) and the modular structures were computed using the algorithm of (Blondel et al., 2008).

Parameter	Description	Value
c_{EE}	Excitatory to excitatory weight	12.0
c_{IE}	Inhibitory to excitatory weight	4.0
c_{EI}	Excitatory to inhibitory weight	13.0
c_{II}	Inhibitory to inhibitory weight	11.0
τ_E	Membrane time-constant, excitatory population	10.0
τ_I	Membrane time-constant, inhibitory population	10.0
a_E	Slope of excitatory response function	1.2
b_E	Position of maximum slope of excitatory sigmoid function	2.8
c_E	Amplitude of excitatory response function	1.0
θ_E	Excitatory threshold	0.0
a_I	Slope of inhibitory response function	1.0
b_I	Position of maximum slope of inhibitory sigmoid function	4.0
θ_I	Inhibitory threshold	0.0
c_I	Amplitude of inhibitory response function	1.0
r_E	Excitatory refractory period	1.0
r_I	Inhibitory refractor period	1.0
k_E	Maximum value of excitatory response function	1.0
k_I	Maximum value of inhibitory response function	1.0
α_E	Balance between excitatory and inhibitory	1.0
α_I	Balance between excitatory and inhibitory	1.0

Table S1. Parameters used in the Wilson-Cowan equation for each connectome node within TVB. The parameters shown above are the default parameters within TVB and are also shown in Table 11(a) of (Sanz-Leon et al., 2015).

Parameter	Value
Number of nodes	998
Global coupling strength	0.15
White matter transmission speed (mm/ms)	3.0
Integrator	Euler stochastic (dt=5)

Table S2. Parameters used for simulating the Hagmann et al. (Hagmann et al., 2008) connectome within the TVB resting state simulator. Please note the values of Global coupling strength and white matter transmission speed above are different to those presented in (Ulloa & Horwitz, 2016). In the present study we implemented a parameter search to better reproduce empirical RS FC of (Hagmann et al., 2008). See methods sections for details.

Parameter	E element	I element
K	9.0	20.0
$\boldsymbol{\phi}$	0.3	0.1
N	$\pm$0.025	$\pm$0.025
Δ	0.5	0.5
$\boldsymbol{\delta}$	0.5	0.5

Table S3. Parameters used in the Wilson-Cowan unit model of each LSNM submodule

Source	Destination	Fanout	Mean/SD	Percent to create	Comments
LGN	V1	7x7	34 @ 0.003±0.003 2 x 5 @ 0.006 ± 0.003 1 x 5 @ 0.020 ± 0.002	100	Highest values oriented either vertically or horizontally
V1h	V4h	1x5	0.04 ± 0.01	50	
V1v	V4v	5x1	0.04 ± 0.01	50	
V1h	V4c	3x3	4 @ 0.0 ± 0.01 5 @ 0.02 ± 0.01	50	Lowest values at the corners
V1v	V4c	3x3	4 @ 0.0 ± 0.01 5 @ 0.02 ± 0.01	50	Lowest values at the corners
V4	IT	5x5	0.01 ± 0.01	50	Learned
IT	FS	1x1	0.2 ± 0.02	100	
D2	V4	5x5	0.0014 ± 0.0007	100	
D1	IT	1x1	0.03 ± 0.001	100	Inhibitory
D2	IT	1x1	0.01 ± 0.002	100	
IT	V4	4x4	0.00125 ± 0.0006	100	

Table S4. Connection patterns among submodules of LSNM model

Source	Destination	Element	Weight
FS	D2	E	0.07
FS	FR	E	0.05
D1	FR	E	0.06
D1	D2	E	0.105
D2	D1	E	0.10
D1	FS	I	0.02
FS	D1	I	0.05
FR	D1	I	0.03
FR	D2	I	0.065

Table S5. Connection weights among submodules in the prefrontal cortex region of LSNM

Parameter	Description	Value	Reference
τ_s	Rate constant of vasodilatory signal decay in seconds	1.54	(Heinzle, Koopmans, den Ouden, Raman, & Stephan, 2016)
τ_f	Time of flow-dependent elimination in seconds	2.44	(Heinzle et al., 2016)
α	Grubb's vessel stiffness exponent	0.32	(Heinzle et al., 2016)
τ_0	Hemodynamic transit time in seconds	2.0	(Havlicek et al., 2015)
ϵ	Efficacy of synaptic activity to induce signal	0.1	(Friston et al., 2000)
r_0	Slope of intravascular relaxation rate in Hertz	108.0	(Havlicek et al., 2015)
ϑ_0	Frequency offset at outer surface of magnetized vessels	80.6	(Obata et al., 2004)
ε	Ratio of intra- and extravascular BOLD signal at rest	0.47	(Heinzle et al., 2016)
V_0	Resting blood volume fraction	0.02	(Obata et al., 2004)
E_0	Resting oxygen extraction fraction	0.34	(Heinzle et al., 2016)
TE	Echo time	0.03	(Heinzle et al., 2016)

Table S6. Parameters used for the Balloon model of hemodynamic response used in our simulations. Values are based on a 3T MRI magnet.